Effects of dust scattering albedo and 2175 A bump on ultraviolet colours of normal disc galaxies

Akio K. Inoue, Veronique Buat, Denis Burgarella, Pasquale Panuzzo, Tsutomu T. Takeuchi, Jorge Iglesias-Paramo

Mon. Not. R. Astron. Soc. **370,** 380–398 (2006) doi:10.1111/j.1365-2966.2006.10499.x

Effects of dust scattering albedo and 2175-Å bump on ultraviolet colours of normal disc galaxies

Akio K. Inoue,[1,2]★ Veronique Buat,[2] Denis Burgarella,[2] Pasquale Panuzzo,[3] Tsutomu T. Takeuchi[2]† and Jorge Iglesias-Páramo[4]

[1]*College of General Education, Osaka Sangyo University, 3-1-1, Nakagaito, Daito, Osaka 574-8530, Japan*
[2]*Laboratoire d'Astrophysique de Marseille, Traverse du Siphon, BP 8, 13376 Marseille, CEDEX 12, France*
[3]*INAF Padova, Vicolo dell'Osservatorio 5, I-35122 Padova, Italy*
[4]*Instituto de Astrofísica de Andalucía (CSIC), 18008 Granada, Spain*

Accepted 2006 April 21. Received 2006 April 17; in original form 2005 November 26

ABSTRACT

We discuss dust properties in the interstellar medium (ISM) of nearby normal galaxies by comparing observations in the ultraviolet (UV) with simulations by a radiative transfer model. The observed UV colours of nearby galaxies show a reddening relative to their expected intrinsic colours. Some authors argued that the Milky Way dust cannot reproduce the reddening because of the prominent 2175-Å absorption bump. Other authors proposed a reduction mechanism of the bump strength in an *attenuation law* derived from the ratio of the observed intensity to the intrinsic one through an age-selective attenuation (i.e. young stars are more attenuated selectively). We find that the wavelength dependence of the scattering albedo also has a strong effect on the UV colour; an albedo decreasing towards shorter wavelengths (except for the absorption bump range) produces a significant UV reddening. After comparing the observed UV colours of nearby normal galaxies with those expected from radiative transfer simulations assumed several dust models, we find two sorts of dust suitable for these galaxies: (i) dust with a bump and a smaller albedo for a shorter wavelength (except for the bump range) and (ii) dust without any bump but with an almost constant albedo. If very small carbonaceous grains responsible for the common unidentified infrared emission band are also the bump carrier, the former dust is favourable. Finally, we derive mean attenuation laws of various dust models as a function of the UV attenuation, and derive some relations between the UV attenuation and observable/theoretical quantities.

Key words: radiative transfer – dust, extinction – galaxies: ISM – infrared: galaxies – ultraviolet: galaxies.

1 INTRODUCTION

Dust grains affect our observations strongly, especially in the ultraviolet (UV) band, through *extinction* (absorption and scattering processes). When we observe galaxies whose stars are not resolved by a telescope, the effects of the radiative transfer, i.e. multiple scatterings and the configuration of dust grains and stars, are also effective. In this paper, we call the effective extinction including such effects *attenuation*.[1] To correctly understand the intrinsic spectrum of galaxies (unresolved into individual stars), we must correct observational data for the dust *attenuation* not for the *extinction*.

Theoretically, to know the dust attenuation through a galactic disc is to solve the equation of the radiative transfer through the disc, assuming the wavelength dependence of average dust properties of absorption and scattering, i.e. the *extinction law*. The most prominent feature in the average extinction law of the Milky Way (MW) is the absorption 'bump' at 2175 Å. We find this feature towards almost all lines of sight in the interstellar medium (ISM) of the MW (e.g. Fitzpatrick 1999), suggesting that the carrier of the bump is quite common in the ISM of the MW. We also find the bump in the average extinction law of the Large Magellanic Cloud (LMC) but not in the average extinction law of the Small Magellanic Cloud (SMC) (e.g. Whittet 2003).

Observationally, the wavelength dependence of the attenuation amount, i.e. the *attenuation law*, has been obtained for nearby UV

★E-mail: akinoue@las.osaka-sandai.ac.jp (AKI)
†Present address: Astronomical Institute, Tohoku University, Aoba, Aramaki, Aoba-ku, Sendai 980–8578, Japan.

[1] Other words are also used in the literature: obscuration, effective extinction and so on [see discussions in Calzetti (2001)].

bright starburst galaxies observed with the *International Ultraviolet Explorer* (*IUE*) satellite (Calzetti, Kinney & Storchi-Bergmann 1994). In an average attenuation law of these galaxies (so-called the Calzetti law), the bump is very weak or absent (Calzetti et al. 1994), although some galaxies in the sample show a sign of the bump in their spectra (Noll & Pierini 2005). Based on a radiative transfer model, Gordon, Calzetti & Witt (1997) and Witt & Gordon (2000) argued that this lack of the bump in the Calzetti law is a sign of the absence of the bump in the extinction law, suggesting the absence of the bump carrier in the starburst region. On the other hand, with another radiative transfer model, GRASIL (Silva et al. 1998), Granato et al. (2000) pointed out that, even if the bump exists in the extinction law, the strength of the bump can be greatly reduced in the attenuation law by a radiative transfer effect coupled with an *age-selective attenuation*, i.e. young stars are more attenuated selectively.

The *IUE* starburst galaxies also show a tight correlation between the observed UV spectral slope (β; $f_\lambda \propto \lambda^{-\beta}$) and the infrared (IR)-to-UV flux ratio (so-called IRX): a redder β for a larger IRX (Calzetti et al. 1994; Meurer, Heckman & Calzetti 1999). Since the IRX relates well to the UV attenuation (Buat & Xu 1996), the correlation means that the UV spectrum (i.e. the UV colour) becomes redder monotonically as the attenuation increases. Witt & Gordon (2000) argued that the UV colour cannot be redden by the extinction law of the MW even if the dust column density of a medium increases. This is because the absorption bump lies in the near-UV (NUV). Indeed, the extinction in the NUV is slightly larger than that in the far-UV (FUV) for the MW extinction law. Their finding again suggests the lack of the bump carrier in the starburst galaxies.

A suggested candidate of the bump carrier is very small carbonaceous grains like polycyclic aromatic hydrocarbons (PAHs; Léger et al. 1989), quenched carbonaceous composites (QCCs; Sakata et al. 1983; Wada et al. 1999) and UV processed hydrogenerated amorphous carbon grains (HACs; Mennella et al. 1998), although this is not settled yet (Whittet 2003; Draine 2003a; Henning, Jäger & Mutschke 2004). These very small carbonaceous particles are confidently attributed to the unidentified infrared (UIR) emission band in 3–13 μm (Léger & Puget 1984; Sakata et al. 1984; Whittet 2003). The UIR emission band is quite common in the ISM of the MW (e.g. Onaka 2004) and of other galaxies (e.g. Genzel & Cesarsky 2000), except for low-metallicity ($\lesssim 1/5\, Z/Z_\odot$) galaxies in which the UIR emission is weak or absent (Engelbracht et al. 2005). If the very small carbonaceous grains producing the UIR emission are really responsible for the bump, we should find the bump in the extinction law of other galaxies (but not so low metallicity). Indeed, the bump has been found in M31 (Bianchi et al. 1996) and some distant galaxies, for example, a lensing galaxy at $z = 0.83$ (Motta et al. 2002) and Mg II absorption systems at $z = 1.5$ (Wang et al. 2004). There are also signs of the bump imprinted in the observed UV spectra of a galaxy at $z = 0.048$ (Burgarella et al. 2005a), of some *IUE* starburst galaxies (Noll & Pierini 2005), and of some star-forming galaxies at $z \sim 2$ (Noll & Pierini 2005).

The amount of the bump carrier may depend on the star-forming activity (Gordon 2005, and references therein). Gordon & Clayton (1998) found one sightline with the bump in the SMC. Interestingly, this sightline is towards a quiescent area in the SMC. Valencic et al. (2003) found one sightline without the bump towards an actively star-forming region (Trumpler 37) in the MW (see also Sofia et al. 2005). Whittet et al. (2004) also found a sightline without the bump towards a molecular cloud in the MW (see also Sofia et al. 2005). Furthermore, the UIR emission flux (possibly related to the bump carrier) relative to the far-IR flux decreases as the intensity of the interstellar radiation field increases (Onaka 2004). Such a bump carrier fragile against the star-forming activity may explain the absence of the bump in the Calzetti law. On the other hand, there is a good correlation between the UIR emission strength and the star-forming activity for starburst galaxies as well as for normal galaxies (Genzel & Cesarsky 2000).

Quiescent or modest star-forming 'normal' galaxies and ultraluminous infrared galaxies (ULIRGs) do not follow the tight correlation of the *IUE* starburst galaxies on the IRX–β diagram (Bell 2002; Goldader et al. 2002). Particularly, normal galaxies show systematically redder UV colours than those of the *IUE* starburst galaxies (Bell 2002; Kong et al. 2004). This fact has recently been confirmed by the *GALEX* satellite (Martin et al. 2005) for larger samples of nearby galaxies selected in the NUV or optical (Buat et al. 2005; Seibert et al. 2005). Resolved star-forming regions (aperture size of 520 pc) in M51 also show the same trend as the normal galaxies on the IRX–UV colour diagram (Calzetti et al. 2005). According to Witt & Gordon (2000), the MW-type dust cannot reproduce even the UV colour of the *IUE* starburst galaxies, much less the redder UV colour of normal galaxies. Does the red UV colour of normal galaxies indicate the lack of the bump carrier in their ISM and suggest different origins of the bump and the UIR emission?

With a simple power-law type attenuation law (i.e. without a bump) as introduced by Charlot & Fall (2000), Kong et al. (2004) claimed that the redder UV colour of normal galaxies is due to a post-burst stellar population if galaxies have an intermittent star formation. They expected a trend that the current star formation rate relative to the past average one (so-called the birthrate parameter) depends on the distance from the starburst relation on the IRX–β diagram. However, the observed trend is weak (Cortese et al. 2006; Panuzzo et al. 2006). In addition, the expected recent burst of nearby galaxies observed with the *GALEX* seems to be too weak to change their UV colours significantly (Burgarella, Buat & Iglesias-Páramo 2005b).

Burgarella et al. (2005b) applied a more realistic attenuation law, i.e. a power-law plus a Gaussian bump to their statistical investigation in order to understand the nature of *GALEX* galaxies. They found that an attenuation law with a bump and a somewhat steep slope is suitable for these galaxies. Such a steep attenuation law is expected from an *age-selective attenuation* (Inoue 2005). More recently, an updated GRASIL model (Panuzzo et al. 2006) very well reproduced the red UV colours of *GALEX* galaxies with the MW-type dust. They adopted a more realistic stellar distribution; younger stars are more deeply embedded in the dust disc, whereas older stars distribute more extensively (e.g. Robin et al. 2003; Zaritsky et al. 2004). This realistic configuration of dust and stars depending on the stellar age produces an *age-selective attenuation*. This results in a steep attenuation law which overcomes the *blueing* by the bump.

In addition to the *age-selective attenuation*, this paper discusses the effect of the wavelength dependence of the scattering albedo on the UV colour. In fact, the dust properties adopted by Witt & Gordon (2000) and the GRASIL are different from each other, especially the wavelength dependence of albedos. This point significantly affects the expected UV colour as shown later (Section 3). Witt & Gordon (2000) empirically derived the wavelength dependence of the albedo from a large compilation of the albedos estimated from observations with radiative transfer models [see Gordon (2004) for a review]. On the other hand, the dust properties adopted in the GRASIL are a theoretical model by Draine and co-workers (Weingartner & Draine 2001; Draine 2003b). Such a difference in the adopted dust models could play a role in the contradictory conclusions from the two groups.

This paper thoroughly examines dust properties in nearby galaxies, in particular the presence of the bump and the wavelength dependence of the albedo, based on the *GALEX* colour. We adopt a one-dimensional plane-parallel radiative transfer model developed by Inoue (2005). While its computational geometry is one-dimensional, this model can treat the clumpiness of stars and dust thanks to the mega-grain approximation (Városi & Dwek 1999). The validity of this approximation has been clearly shown by Városi & Dwek (1999) who compared the approximation with a three-dimensional Monte Carlo radiative transfer. Owing to the computational cheapness of the one-dimensional calculation, we can investigate a very wide range of physical quantities of disc galaxies.

In the next section, we present a description of the radiative transfer model, detailed explanations of the dust models and the setup of the plane-parallel discs. The main results and discussions are presented in Section 3 where we search suitable dust models for nearby 'normal' galaxies. In Section 4, we derive mean attenuation laws as a function of the UV attenuation for future use. The final section is a summary of our conclusions.

2 RADIATIVE TRANSFER THROUGH A GALACTIC DISC

In this paper, we use a one-dimensional plane-parallel radiative transfer model through a galactic disc with clumpy distributions of stars and dust developed by Inoue (2005). The clumpiness of the medium (i.e. the dust distribution) is treated by the mega-grain approximation which was first proposed by Neufeld (1991) and further developed by Hobson & Padman (1993) and Városi & Dwek (1999). In this approximation, we regard a dusty clump as a huge particle producing absorption and scattering effects like a normal single dust grain. We note that Városi & Dwek (1999) clearly show the validity of the approximation by comparisons between the approximate solutions and their three-dimensional Monte Carlo radiative transfer solutions. The radiative transfer code of Inoue (2005) can also treat a smooth medium if we do not use the mega-grain approximation. Since the global geometry is one-dimensional plane-parallel, we do not consider the bulge and the radial structure of the disc.

By solving the radiative transfer equations in a single configuration of stars and dust, we obtain a transmission rate curve, T_λ, which is the ratio of the observable and the intrinsic intensities as a function of the wavelength, λ. When there are some stellar populations with different configurations relative to dust in a galactic disc, the total transmission rate through the disc is (e.g. Tuffs et al. 2004)

$$T_\lambda = \sum_i f_{i,\lambda} T_{i,\lambda}, \tag{1}$$

where $T_{i,\lambda}$ is the transmission rate through the ith configuration and $f_{i,\lambda}$ is the luminosity weight of the ith stellar population with a normalization of $\sum_i f_{i,\lambda} = 1$. Equation (1) means that we can solve the radiative transfer equations for each stellar population (with each configuration relative to dust) independently. To obtain the total transmission rate, we simply sum all the transmission rates with luminosity weights (Section 2.4).

The transmission rate of each configuration $T_{i,\lambda}$ depends on (i) the dust model, (ii) the ISM model and (iii) the stellar distribution. If we divide stars into some populations depending on their age, the luminosity weight $f_{i,\lambda}$ is determined by (i) the age criteria and (ii) the star formation history (SFH).

In the following, we describe the dust models considered here (Section 2.1), the ISM model (Section 2.2) and the stellar populations and distributions (Section 2.3). Then, we describe how to composite these populations (Section 2.4).

Table 1. Dust models.

Model	Reference	$k^a_{\mathrm{d},V}$
MW (WG dust)	Witt & Gordon (2000)	2.60×10^4
SMC (WG dust)	Witt & Gordon (2000)	1.56×10^4
MW (Draine dust)	Draine (2003b)	2.60×10^4
SMC (Draine dust)	Weingartner & Draine (2001)	1.56×10^4
LMC av (Draine dust)	Weingartner & Draine (2001)	1.95×10^4
LMC 2 (Draine dust)	Weingartner & Draine (2001)	1.89×10^4

[a]Visual extinction cross-section per unit dust mass (cm^2 g^{-1}).

2.1 Dust models

We consider six dust models in this paper. Table 1 is a summary of the models and their references. There are two origins of these models; one is an empirical model by Witt & Gordon (2000) (hereafter WG dust) and the other is a theoretical model by Weingartner & Draine (2001) and Draine (2003b) (hereafter Draine dust). There are also four types of dust compositions: the MW, the SMC and the two different LMC types (LMC av and LMC 2). The LMC av type is an average dust composition over many sightlines towards the LMC, except for the supershell region around the 30 Doradus, and the LMC 2 type is the dust composition towards the supershell. In the Draine dust, the bump is assumed to be produced by very small carbonaceous particles including the 'astronomical' PAHs designed to fit observations (Li & Draine 2001).

Fig. 1 shows the extinction cross-sections (panel a) and the albedos (panel b) of these models as a function of the wavelength. The

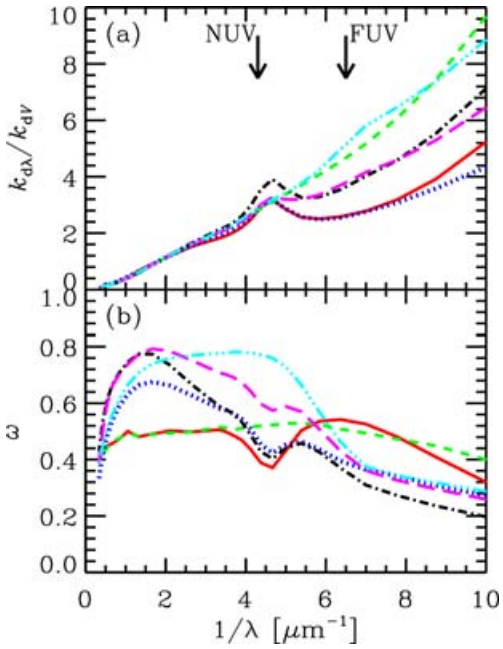

Figure 1. Differences of dust models. The panel (a) shows the extinction laws (extinction cross-sections normalized by those at the V band) and the panel (b) shows the albedos. The solid and short-dashed lines are the MW and the SMC types of Witt & Gordon (2000), respectively. The dotted, dot–dashed, long-dashed and three-dots–dashed lines are the MW, the LMC av, the LMC 2 and the SMC types of Draine (2003b) and Weingartner & Draine (2001), respectively. The two downwards arrows in the panel (a) show the effective wavelengths of the two *GALEX* filters.

extinction cross-sections (i.e. extinction laws) are very similar between the WG dust and the Draine dust if we compare the same composition type. We find a prominent bump at 0.22 μm ($1/\lambda = 4.6\,\mu\mathrm{m}^{-1}$) in the MW and the LMC av types, a weak bump in the LMC 2 type and no bump in the SMC type. We note here that the LMC av type has a rather strong bump (Fitzpatrick 1986; Misselt, Clayton & Gordon 1999).

On the other hand, the albedos are very different between the WG dust and the Draine dust (panel b). Except for the bump region, albedos of the WG dust (solid and dashed lines) show a flat wavelength dependence in $2\,\mu\mathrm{m}^{-1} < 1/\lambda < 8\,\mu\mathrm{m}^{-1}$, whereas those of the Draine dust (other lines) show a rapid decrease towards shorter wavelengths. This different wavelength dependence of the albedo significantly affects the UV colour as shown later (Section 3).

In Fig. 2, we show comparisons between albedos of the MW-type dusts and those estimated from observations of the diffuse Galactic light (panel a), of the reflection nebulae (panel b) and of the dark clouds (panel c) (see also Gordon 2004). Since the estimated values show a large dispersion and both dust models are still compatible with the data, we cannot judge which model is better.

2.2 ISM models

We consider two cases of the ISM, smooth and clumpy, in a plane-parallel disc. We do not consider any systematic vertical structure of the disc; the mean gas (dust) density is constant along the vertical axis from the equatorial plane to a height h_d. Above this height, nothing produces absorption and scattering. For a clumpy medium, we have clumps distributed randomly in the gas disc, keeping the constant gas density in a volume average.

To model the clumpy medium, we assume a multiphase ISM picture (e.g. Field, Goldsmith & Habing 1969, see section 2 in Inoue 2005 for details). Assuming the thermal energy and chemical equilibria in the ISM with temperatures lower than 10^4 K, we have two thermally stable phases (see Fig. 3): the warm neutral medium (WNM) and the cold neutral medium (CNM). They are regarded as the inter-clump medium and clumps, respectively. Based on Wolfire et al. (2003), we adopt analytical approximations of the relations between the thermal pressure and the density of these two phases as

$$\frac{p/k_\mathrm{B}}{10^4\,\mathrm{K\,cm^{-3}}} = \frac{n_\mathrm{H,wnm}}{1\,\mathrm{cm^{-3}}} \quad \text{(WNM)} \tag{2}$$

and

$$\frac{p/k_\mathrm{B}}{10^{4.5}\,\mathrm{K\,cm^{-3}}} = \left(\frac{n_\mathrm{H,cnm}}{10^3\,\mathrm{cm^{-3}}}\right)^{0.7} \quad \text{(CNM)}. \tag{3}$$

They are shown in Fig. 3 as solid lines. By assuming a mean thermal pressure, we have a corresponding density contrast between the two phases. We also assume a mean density of the ISM to obtain a volume filling factor of clumps. Finally, the clumps are assumed to be self-gravitating in order to specify their radius (i.e. the Jeans length).

In order to compare the models with observed galaxies and to extract the information of dust properties, we cover a wide range of physical quantities of disc galaxies: the mean ISM hydrogen density ($n_\mathrm{H} = 0.5$–$24\ \mathrm{cm^{-3}}$), the half height of the dusty disc ($h_\mathrm{d} = 50$–300 pc), the dust-to-gas mass ratio ($\mathcal{D} = 0.001$–0.01) and the mean ISM thermal pressure ($p_\mathrm{th}/k_\mathrm{B} = 10^{3.0-4.0}\ \mathrm{K\,cm^{-3}}$), which are summarized in Table 2. When we keep the two phases described above, allowed densities are restricted between the two solid lines in Fig. 3 for a fixed thermal pressure. Thus, we can take $n_\mathrm{H} = 0.5$–$6.0\ \mathrm{cm^{-3}}$ for $p_\mathrm{th}/k_\mathrm{B} = 10^{3.0}\ \mathrm{K\,cm^{-3}}$ and $n_\mathrm{H} = 2.0$–$24.0\ \mathrm{cm^{-3}}$ for $p_\mathrm{th}/k_\mathrm{B} = 10^{4.0}\ \mathrm{K\,cm^{-3}}$. For $p_\mathrm{th}/k_\mathrm{B} = 10^{3.5}\ \mathrm{K\,cm^{-3}}$, we can take all the values of n_H listed in Table 2. Consequently, we have 504 sets of parameters for the clumpy ISM.

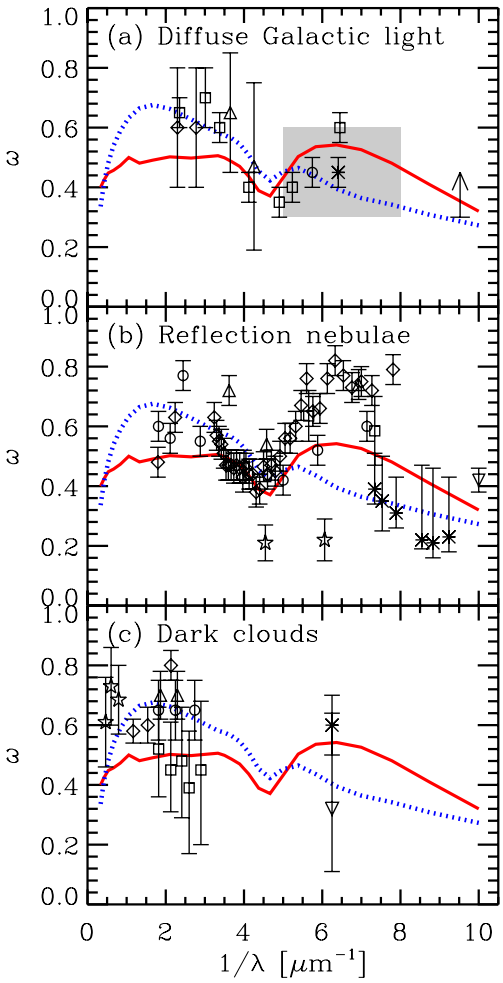

Figure 2. Albedos estimated in the ISM of the MW. (a) The diffuse Galactic light; diamonds: Mathis (1973); squares: Lillie & Witt (1976); triangles: Morgan, Nandy & Thompson (1976); arrow (lower limit): Murthy et al. (1993); shaded area: Murthy & Henry (1995); circle: Witt, Friedmann & Sassen (1997) and asterisk: Schiminovich et al. (2001). (b) The reflection nebulae; circles: Witt et al. (1982); triangles: Witt et al. (1992); inverse-triangle: Witt et al. (1993); squares: Gordon et al. (1994); diamonds: Calzetti et al. (1995); asterisks: Burgh, McCandliss & Feldman (2002) and stars: Gibson & Nordsieck (2003). (c) The dark clouds; circles: Mattila (1970); triangles: Fitzgerald, Stephens & Witt (1976); squares: Laureijs, Mattila & Schnur (1987); diamonds: Witt, Oliveri & Schild (1990); asterisk: Hurwitz (1994); inverse-triangle: Halkala et al. (1995) and stars: Lehtinen & Mattila (1996). The solid and dotted lines are the dust models for the MW by Witt & Gordon (2000) and Draine (2003b), respectively.

In a smooth ISM compared with the clumpy ISM later, we do not need to specify the ISM thermal pressure because we do not make the two-phase medium. Hence, we have 216 sets of parameters for the smooth ISM.

As pointed out by Dopita et al. (2005), the ISM pressure affects the size of H II regions and the dust temperature in and around these regions. Since we do not consider the spectral shape of the dust IR emission in this paper, we omit this effect. In starburst galaxies, a very high ISM pressure like $p_\mathrm{th}/k_\mathrm{B} = 10^6\ \mathrm{K\,cm^{-3}}$ is observed (Lord et al. 1996; Heckman et al. 1999). However, the two-phase equilibrium is not established in such a high ISM pressure as shown

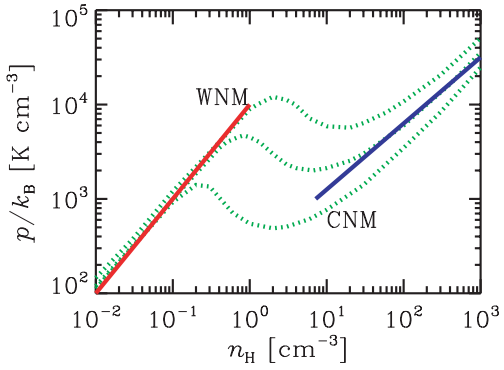

Figure 3. Phase diagram: thermal pressure–hydrogen number density. The dotted curves indicate the thermal equilibrium points in the ISM of the MW (top: Galactocentric radius of 3 kpc, middle: 8.5 kpc, and bottom: 15 kpc) reproduced from fig. 7 of Wolfire et al. (2003). The two solid lines are the approximate relations of two thermally stable phases, the WNM and the CNM, as expressed in equations (2) and (3).

Table 2. Considered physical quantities of the ISM.

Quantity	Values	Unit
$p_{\rm th}/k_{\rm B}{}^a$	$10^{3.0}$, $10^{3.5}$, $10^{4.0}$	K cm^{-3}
D^b	10^{-3}, $10^{-2.5}$, 10^{-2}	...
$n_{\rm H}{}^c$	0.5, 0.75, 1.0, 1.5, 2.0, 3.0, 4.0, 6.0, 8.0, 12.0, 16.0, 24.0	cm^{-3}
$h_{\rm d}{}^d$	50, 100, 150, 200, 250, 300	pc

[a]Mean thermal pressure.
[b]Dust-to-gas mass ratio.
[c]Mean hydrogen density.
[d]Half height of the dusty gas disc.

in Fig. 3 (there is no branch of the WNM solution). Since we stand on the two-phase model, we restrict ourselves within the range of $p_{\rm th}/k_{\rm B} = 10^{3.0-4.0}$ K cm^{-3} which is observed in the ISM of MW (Myers 1978). Thus, our model is for the 'normal' galaxies in this respect.

The total disc optical depth at the visual band (0.55 μm) along the normal of the disc is

$$\tau_V = 0.2 \left(\frac{k_{{\rm d},V}}{10^4\,{\rm cm^2\,g^{-1}}}\right)\left(\frac{n_{\rm H}}{1\,{\rm cm^{-3}}}\right)\left(\frac{h_{\rm d}}{150\,{\rm pc}}\right)\left(\frac{\mathcal{D}}{10^{-2}}\right). \quad (4)$$

We note that this optical depth is not observable because it is just proportional to the input dust column density and does not include the radiative transfer effect. With the visual extinction cross-section per unit dust mass, $k_{{\rm d},V}$, given in Table 1, the considered range of the input optical depth along the normal axis of the discs is 0.005–25, which corresponds to 0.002–5 $M_\odot$ pc^{-2} in terms of the dust column density (see also Section 4.2.3).

2.3 Stellar populations and their distributions

First, we consider an age-dependent scaleheight of the stellar distribution. In the MW, the scaleheight of stars younger than 0.1–1 Gyr is ∼50 pc, whereas the scaleheight of the older stars is ∼300 pc (Binney & Merrifield 1998; Robin et al. 2003). This is an observational fact, although the origin of this age-dependent height is still controversial (Spitzer & Schwarzschild 1951; Tinsley & Larson 1978; Rana 1991; Rocha-Pinto et al. 2004). Since the scaleheight of the neutral hydrogen is about 150 pc (Binney & Merrifield 1998), we have the layering parameters (ratio of the dusty disc height $h_{\rm d}$ to the stellar scaleheight h_*) of ∼3 for younger stars and of ∼0.5 for older stars. We simply set these layering parameters to be constant when the height of the dusty disc changes in our model.

Table 3. Properties of the stellar populations.

Population	Age	Layering parameter	Distribution
Young	< 10 Myr	3.0	Clumpy/smooth
Intermediate	10–300 Myr	3.0/0.5	Smooth
Old	> 300 Myr	0.5	Smooth
Age of galaxies		10 Gyr	
e-folding time of the SFH		5 Gyr	

Next, we divide the younger population into two groups. Observationally, the youngest stars are often associated with the molecular clouds. This is natural because stars are formed in the molecular clouds. On the other hand, this means very inhomogeneous distribution of the youngest stars. To take into account such a clumpy stellar distribution, we bury the youngest stars into clumps in the ISM described in the previous section. Eventually, we have three stellar populations which are called *young*, *intermediate* and *old* stellar populations in this paper (Table 3).

Then, we introduce the age criteria of these three stellar populations. The young stellar population is the population embedded in clumps (i.e. molecular clouds). Thus, a possible age criterion for this population is a lifetime of molecular clouds, for example, 10 Myr (e.g. Blitz & Shu 1980). This time-scale is also similar to the lifetime of the latest O type stars. On the other hand, a comparison between the number of the (ultra)compact HII regions (i.e. embedded massive stars) and the number of the visible O stars suggests that only 10–20 per cent of all O type stars are deeply embedded in molecular clouds (Wood & Churchwell 1989). To take into account this fact, we assume a uniform distribution of young stars in a clump. That is, we have young stars near the surface of the clump as well as young stars deeply embedded. The former stars would correspond to visible O type stars. The intermediate population has a smaller scaleheight than that of old stars. Thus, the age criterion for this population is determined by the observed age-dependence of the scaleheight. According to Robin et al. (2003), stars with an age of 0.1–1 Gyr have the smallest scaleheight. Here, we adopt 300 Myr for the criterion. This is similar to the time-scale to reach the stationarity in the UV flux for a continuous star formation.

Table 3 is a summary of the adopted properties of the stellar populations. To discuss the effect of the clumpiness of the young population, we consider a smooth distribution for this population in addition to a clumpy distribution. We also consider two scaleheights (i.e. two layering parameters) for the intermediate population in order to discuss the effect of the small scaleheight of this population.

With the age criteria described above, we have luminosity fractions of the three stellar populations if we assume a SFH and a spectral energy distribution (SED) of a simple stellar population (SSP). Here, we assume three exponentially decaying SFHs with e-folding time-scales of 1, 3 and 5 Gyr, and a constant SFH. Fig. 4 shows luminosity fractions for the young stars (panel a) and for the intermediate stars (panel b). The age of the galaxy is always assumed to be 10 Gyr. We have used the SEDs of the SSP with the solar metallicity and a Salpeter initial mass function (0.1–100 $M_\odot$) based on the Padova track used in the GRASIL (Silva et al. 1998). For an e-folding time larger than about 3 Gyr, differences are small,

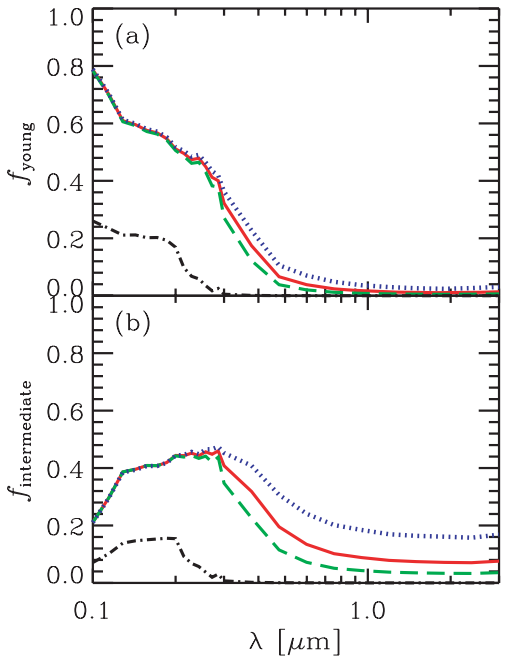

Figure 4. Luminosity fractions of (a) the young and (b) the intermediate stellar populations. The young stars have an age less than 10 Myr, and the intermediate stars have an age between 10 and 300 Myr. The dotted line is the case of a constant star formation rate. The solid, dashed and dot–dashed lines are the cases of an exponential star formation history with a decaying time-scale of 5, 3 and 1 Gyr, respectively. The galactic age of 10 Gyr is assumed for all the cases.

especially at a wavelength less than 0.3 μm. Hereafter, we consider the case of the e-folding time-scale of 5 Gyr (solid line) as a typical case.

We comment on a small feature at around 0.3 μm seen especially in panel (b). This is probably due to the Mg I λ2852 absorption line produced in old stars' atmosphere (e.g. Ponder et al. 1998). This line is not prominent in the atmosphere of younger stars, so that the luminosity fractions of the young stars and the intermediate stars become relatively large. Our grid of the wavelength has only 25 points (see Tables C1–C6), and the grid point at $\lambda = 0.286$ μm is affected by the Mg I line. If our wavelength resolution were higher, more other features would be seen. This point is again discussed in Section 4.1.

In computations of the radiative transfer, the emissivity decreases exponentially along the vertical axis with a scaleheight h_* for the smooth stellar distribution. For the clumpy stellar distribution, the emissivity is locally reduced by multiplying a factor P_{esc} which is the escape energy fraction from a clump (see equation 10 in Inoue 2005). Here, we use an advanced version of the model by Inoue (2005); we take into account the exponentially decreasing distribution with a scaleheight h_* for stars embedded in clumps. We describe the formulation of this improvement in Appendix A. Above the disc height h_d, there are no stars for the clumpy case because of the absence of clumps.

2.4 Composite of star/dust configurations

Now, we composite the three stellar populations introduced in the previous section. This is done by equation (1). We call the dust/star geometry for a single stellar population 'configuration', and call a combination of three stellar populations with different configurations 'composite model'. Considering composite models, we have three points to choose the setup: the clumpy/smooth ISM, the clumpy/smooth young stellar distribution and the small/large scaleheight for the intermediate stellar population. Here, we consider four composite models listed in the top part of Table 4. First, as a standard model, we consider the case with the clumpy ISM, the clumpy young stellar distribution and the small scaleheight of the intermediate stellar population. This case is called 'CCS'. To examine the effect of the scaleheight of the intermediate population, we consider the case with the clumpy ISM, the clumpy young stellar distribution and the large scaleheight of the intermediate population. This is called 'CCL'. To assess the effect of the young stellar distribution, we consider the case with the clumpy ISM, the smooth distribution of the young stars and the small scaleheight of the intermediate stars. This is called 'CSS'. Finally, we consider the case with the smooth ISM, the smooth distribution of the young stars and the small scaleheight of the intermediate stars, which is useful to discuss the effect of the ISM clumpiness and is called 'SSS'.

To produce these four composite models, we need five configurations of dust and stars. In the bottom part of Table 4, a summary

Table 4. Composite models and configurations of dust and stars.

Composite model	CCS	CCL	CSS	SSS	
ISM	Clumpy	Clumpy	Clumpy	Smooth	
Young stellar distribution	Clumpy	Clumpy	Smooth	Smooth	
Scaleheight of intermediate stars	Small	Large	Small	Small	
Composite model	CCS	CCL	CSS	SSS	
Young	ccl3	ccl3	csl3	ssl3	
Intermediate	csl3	csl05	csl3	ssl3	
Old	csl05	csl05	csl05	ssl05	
Configuration	ccl3	csl3	csl05	ssl3	ssl05
ISM	Clumpy	Clumpy	Clumpy	Smooth	Smooth
Stellar distribution	Clumpy	Smooth	Smooth	Smooth	Smooth
Layering parameter[a]	3.0	3.0	0.5	3.0	0.5

[a]Ratio of the height of the dusty disc to the scaleheight of the stellar distribution.

of these configurations is given. The first case is the clumpy ISM, the clumpy stellar distribution and the layering parameter of 3.0 (i.e. smaller scaleheight of the stellar distribution than the height of the dusty disc). This is called 'ccl3' and refers to the young stellar population in the CCS and the CCL models. The next is the clumpy ISM, the smooth stellar distribution and the layering parameter of 3.0. This is called 'csl3' and refers to the intermediate population in the CCS model and the young and intermediate populations in the CSS model. The third is the clumpy ISM, the smooth stellar distribution and the layering parameter of 0.5 (i.e. larger scaleheight of the stellar distribution than the height of the dusty disc). This is called 'csl05' and refers to the intermediate and old populations in the CCL model and the old stellar population in the CCS and CSS models. The fourth is the smooth ISM, the smooth stellar distribution and the layering parameter of 3.0. This is called 'ssl3' and refers to the young and intermediate populations in the SSS model. The last one is the smooth ISM, the smooth stellar distribution and the layering parameter of 0.5. This is called 'ssl05' and refers to the old stellar population in the SSS model. The middle of Table 4 shows correspondences between the configurations and the stellar populations in the composite models.[2]

3 *GALEX* COLOURS AND DUST PROPERTIES

In this section, we show that the *GALEX* colour is strongly affected by dust models, especially by the presence of the bump and by the wavelength dependence of the albedo, rather than by the geometry in the radiative transfer. First, differences among the configurations (Section 3.1) and the composite models (Section 3.2) are shown, and then the suitable dust models for the galaxies observed with the *GALEX* are discussed (Section 3.3). We note here that the filter transmission efficiencies of the *GALEX* two band passes are correctly taken into account in all calculations.

3.1 Comparison of configurations

Here, we compare the UV dust attenuations among different configurations (the bottom part of Table 4) and dust models. To concentrate on effects of dust models and configurations, we consider the colour excess of the two *GALEX* bands, $E(\mathrm{FUV–NUV}) = A_{\mathrm{FUV}} - A_{\mathrm{NUV}}$. Its dependence on the assumed SED is very weak (we assume a flat SED, $f_\lambda \propto \lambda^0$, for simplicity in this Section and in Section 3.2). Fig. 5 shows the FUV attenuation, A_{FUV}, as a function of $E(\mathrm{FUV–NUV})$. The panels (a)–(f) correspond to the six dust models described in Section 2.1. In each panel, the solid line is the locus expected from the extinction law (i.e. distant uniform screen geometry) and the dashed line is that from the Calzetti law. When preparing the figure, we calculated A_{FUV} and A_{NUV} [and then $E(\mathrm{FUV\text{-}NUV})$] from the transmission rate curves obtained from the radiative transfer calculations with each configuration. Thus, we had 48 384 (8,064 × 6 dusts) points each for csl05, csl3 and ccl3 (clumpy ISM cases) and 20 736 (3,456 × 6 dusts) points each for ssl05 and ssl3 (smooth ISM cases) on the $E(\mathrm{FUV–NUV})$ –A_{FUV} plane. Then, we divided these points into several bins in A_{FUV} and obtained the maximum, minimum and median values of the distribution of $E(\mathrm{FUV–NUV})$ for each bin, each dust and each configuration. The plotted symbols indicate the median location for five configurations: diamonds, squares, open circles, triangles and filled circles are ssl05, ssl3, csl05, csl3 and ccl3, respectively. The bin-widths are shown as the vertical error-bars, and the full distribution ranges of $E(\mathrm{FUV–NUV})$ are shown as the horizontal error-bars.

Through all the panels, we see a large variation of the plotted points depending on the dust models. From comparisons between the MW and SMC types (a and b, or c and d), we find the effect of the bump is very large; the most of the MW cases distribute within $|E(\mathrm{FUV} - \mathrm{NUV})| \lesssim 0.3$ mag because of the bump, whereas the SMC cases can reach at $E(\mathrm{FUV–NUV}) \gtrsim 0.5$ mag. Indeed, we see *'blueing'* due to the bump in the MW (WG dust) case (panel a). The LMC cases (panels e and f) are located between the MW and the SMC cases. Thus, we observe the trend that the UV colour becomes redder as the bump becomes weaker (e.g. Witt & Gordon 2000).

We find that the wavelength dependence of the albedo also strongly affects the UV colour. From comparisons between two dust models with the same extinction law (a and c, or b and d), we find that the Draine dust cases are systematically redder than the WG dust cases. Indeed, the MW (WG dust) case shows blueing, whereas the MW (Draine dust) case shows a slight reddening. While most of the points of the WG dust appear in the left-hand side (bluer colour) of the extinction law (solid line), those of the Draine dust are in the right-hand side (redder colour) of the extinction law, except for some large A_{FUV} cases. This difference is caused by the difference in albedos. As shown in Fig. 1(b), the albedos of the Draine dusts decrease rapidly from optical to UV. On the other hand, those of the WG dusts are almost flat, except for the bump domain. Relative to the WG dusts, the Draine dusts easily absorb the FUV photons and scatter out the NUV photons, so that the *GALEX* colour becomes redder, i.e. $E(\mathrm{FUV–NUV})$ becomes larger.

In each panel, we compare the different configurations. All configurations, except for the ccl3, show a maximum in A_{FUV} and a turnover of $E(\mathrm{FUV–NUV})$ in the middle of their locus. At the largest A_{FUV}, the minimum $E(\mathrm{FUV–NUV})$ [or maximum for the MW (WG dust) case] reaches 0 mag, i.e. no reddening/blueing.[3] Generally, the observed intensity along a ray is determined by the sum of two intensities along the ray: the intensity transmitted through the dusty disc and the intensity from the source outside the dusty disc (see equation 21 in Inoue 2005). If the disc opacity increases, the first intensity decreases, and the observed intensity is dominated by the second intensity. In this case, the transmission rate (the ratio of the observed to intrinsic intensities) reaches an asymptotic value depending on the relative fraction of the second intensity in the intrinsic total intensity, i.e. the relative amount of the source outside the dusty disc. The maximum A_{FUV} is originated from the asymptotic value. Only the layering parameter determines the amount of the source outside the disc when we consider a single configuration. Thus, the wavelength dependence of the transmission rate disappears (i.e. a grey attenuation), and then we have $E(\mathrm{FUV–NUV}) = 0$ at the maximum A_{FUV}. The ccl3 case has no source outside the dusty disc because

[2] For each configuration, we consider six dust models (Section 2.1) and 504 sets of physical quantities in a clumpy ISM or 216 sets in a smooth ISM (Section 2.2). In total, we have 3,024 cases for each csl05, csl3 and ccl3, and 1,296 cases for each ssl05 and ssl3. After solving the radiative transfer equation with the number of the angular coordinate of 16, we have 48 384 transmission rate curves (T_λ, transmission rates as a function of the wavelength whose resolution of 25 from 0.1 to 3.0 μm) for each csl05, csl3 and ccl3, and 20 736 for each ssl05 and ssl3. Finally, we composite T_λ of these configurations with luminosity weights as shown in Fig. 4 and obtain 48 384 composite T_λ for each CCS, CCL and CSS cases, and 20 736 for the SSS case. In total, we have 165 888 transmission rate curves for the four composite models.

[3] The displacements of the symbol location from $E(\mathrm{FUV–NUV}) = 0$ at the largest A_{FUV} in Fig. 5 are due to the binning effect. Note that the symbol location is median of the $E(\mathrm{FUV–NUV})$ distribution in each bin.

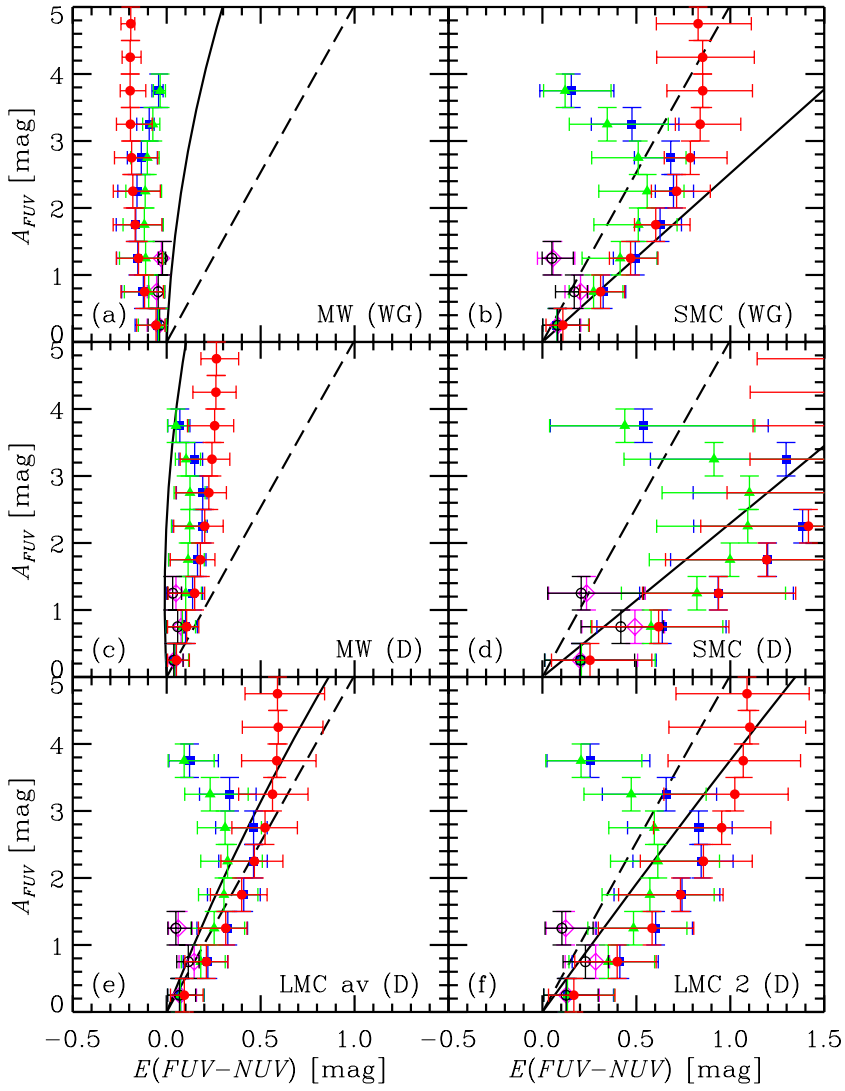

Figure 5. FUV attenuation $A_{\rm FUV}$ as a function of the colour excess E(FUV–NUV). The solid lines are the relation expected from the extinction law (i.e. distant uniform screen). The dashed lines are the case of the Calzetti law. The open diamonds, filled squares, open circles, filled triangles and filled circles are configurations of ssl05, ssl3, csl05, csl3 and ccl3, respectively (see Table 4). The vertical error-bars show the binwidths, the horizontal error-bars show the full widths of the distribution of E(FUV–NUV) in each bin, and the symbols show the median locations of the distribution.

there is no clump outside the disc. Thus, this case does not have the maximum $A_{\rm FUV}$ and shows only a weak turnover outside the plotted region.

The clumpy ISM cases without the embedded stars (csl3 and csl05) are ∼0.1–0.3 mag bluer [redder for the MW (WG dust) case] than the smooth ISM cases (ssl3 and ssl05). This is because a clumpy ISM is less opaque than a smooth ISM. However, the case with the embedded stars (ccl3) has an additional local opacity due to clumps which redden [blue for the MW (WG dust) case] the UV colour, so that its colour excess coincides with the smooth ISM case (ssl3) before the turnover in E(FUV–NUV) (a small $A_{\rm FUV}$) and becomes redder [bluer for the MW (WG dust) case] than the smooth case after the turnover (a large $A_{\rm FUV}$).

In summary, the presence of the bump and the UV wavelength dependence of the albedo strongly affect the UV colour. Except for the case with the embedded stars, the layering parameter puts the maximum UV attenuation at which the colour excess becomes zero. There is also the maximum (or minimum for the blueing case) colour excess. The effects of the ISM clumpiness and the stellar clumpiness are not very large before the maximum colour excess.

3.2 Comparison of composite models

Here, we compare the *GALEX* colour excess, E(FUV–NUV), expected from the composite models summarized in the top part of Table 4. Fig. 6 is prepared by the same way as Fig. 5 and shows the relation between E(FUV–NUV) and $A_{\rm FUV}$. Each composite model is shown by a symbol: SSS (squares), CSS (triangles), CCL (open circles) and CCS (filled circles). Six panels, (a)–(f), show six dust models considered here.

As found in Fig. 5, we find that the effect of the bump is large from comparisons between panels (a and b) or (c and d) and that the wavelength dependence of the albedo is also important from comparisons between panels (a and c) or (b and d), particularly for $A_{\rm FUV} \lesssim 3$ mag. Indeed, E(FUV–NUV) of the MW types (a and c) is about 0.5–1.0 mag bluer than that of the SMC types (b and d).

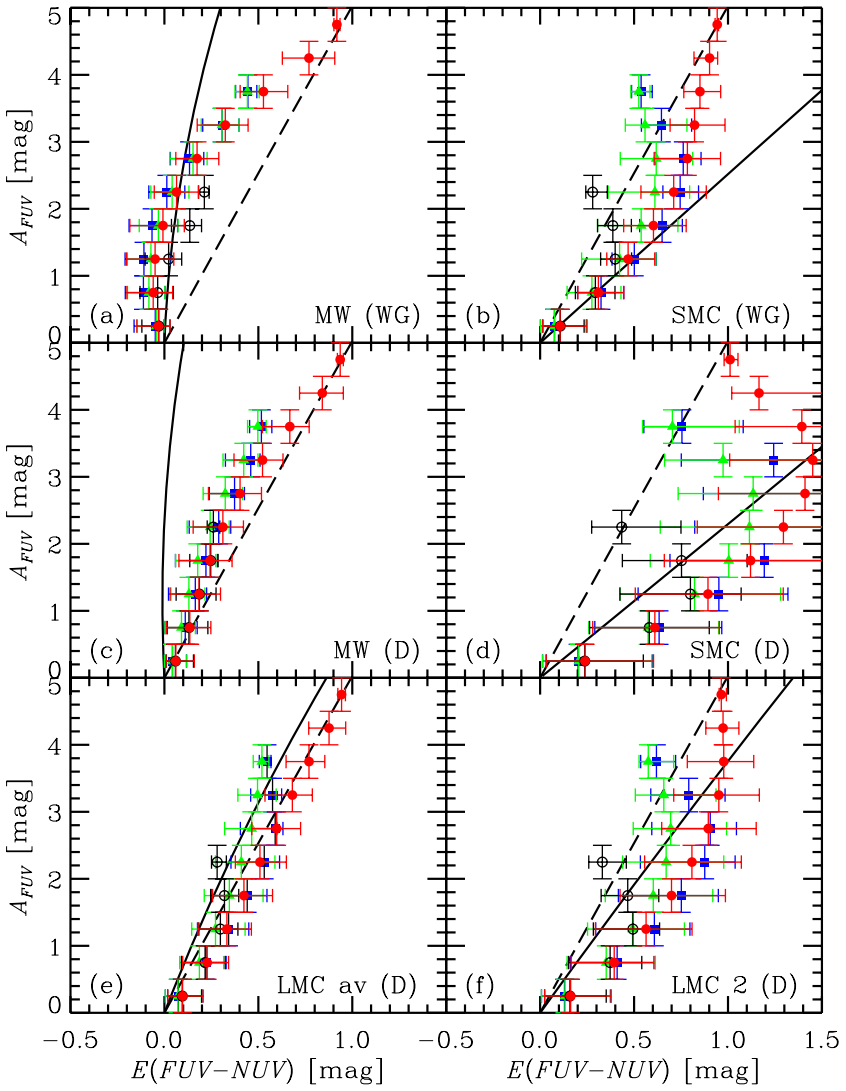

Figure 6. Same as Fig. 5, but composite cases. The filled squares, filled triangles, open circles and filled circles are the SSS, CSS, CCL and CCS models (see Table 4), respectively.

This is the effect of the bump. On the other hand, E(FUV–NUV) of the Draine dusts (c and d) is about 0.2–0.5 mag redder than that of the WG dusts (a and b). This is the effect of the albedo. Thus, the rapidly decreasing albedo towards shorter wavelengths like the Draine dust can partially compensate the blueing effect of the bump.

As seen in Fig. 5, we observe a turnover in E(FUV–NUV) for some cases. However, the final points (the largest $A_{\rm FUV}$) in each composite model do not reach E(FUV–NUV) = 0. This shift from E(FUV–NUV) = 0 is caused by the composite process, i.e. the effect of the age-dependent attenuation. This effect can be understood by equation (1). If the disc opacity is large enough, the attenuations for any populations become grey; $T_{i,\lambda}$ loses the wavelength dependence. Even in this case, we still have the wavelength dependence of $f_{i,\lambda}$. Thus, E(FUV–NUV) for an opaque disc is determined by the wavelength dependence of the luminosity weight, in other words, the SFH and the age criteria of the stellar populations. More interestingly, the attenuation law becomes independent of the dust model in such a case. Indeed, we find that the locations of the largest $A_{\rm FUV}$ point of each composite model in six panels (i.e. six dust models) are very similar to each other. This causes rather large E(FUV–NUV) even for the MW dust (panels a and c). We can expect a red *GALEX* colour even with the bump (see also Panuzzo et al. 2006). The age-dependent attenuation reduces the effect of the bump through the wavelength dependence of the luminosity weights.

In each panel, when we compare the CCS and CCL models, the effect of the intermediate population can be understood. With a large scaleheight of the intermediate population (CCL), we cannot reach $A_{\rm FUV} \gtrsim 2.5$ mag, whereas we reach $A_{\rm FUV} \sim 5$ mag with a small scaleheight of the population. As shown by Buat et al. (2005), FUV attenuations of many nearby galaxies selected by FIR are more than 2.5 mag. Thus, an intermediate population with a small scaleheight is likely to be required. When we compare the CCS and CSS or SSS models, we find the effect of the clumpy young stars. Because of the additional local opacity due to clumps, the CCS model reaches $\sim$1 mag larger $A_{\rm FUV}$ than the CSS and SSS models. We find that the effect of the ISM clumpiness is small for $A_{\rm FUV} \lesssim 3$ mag from a comparison between the CSS and SSS models. In the following discussions, we deal with only the CCS model which consists of the young population embedded in clumps, the intermediate population with a small scaleheight and the old population with a large scaleheight, i.e. the most realistic model in this paper.

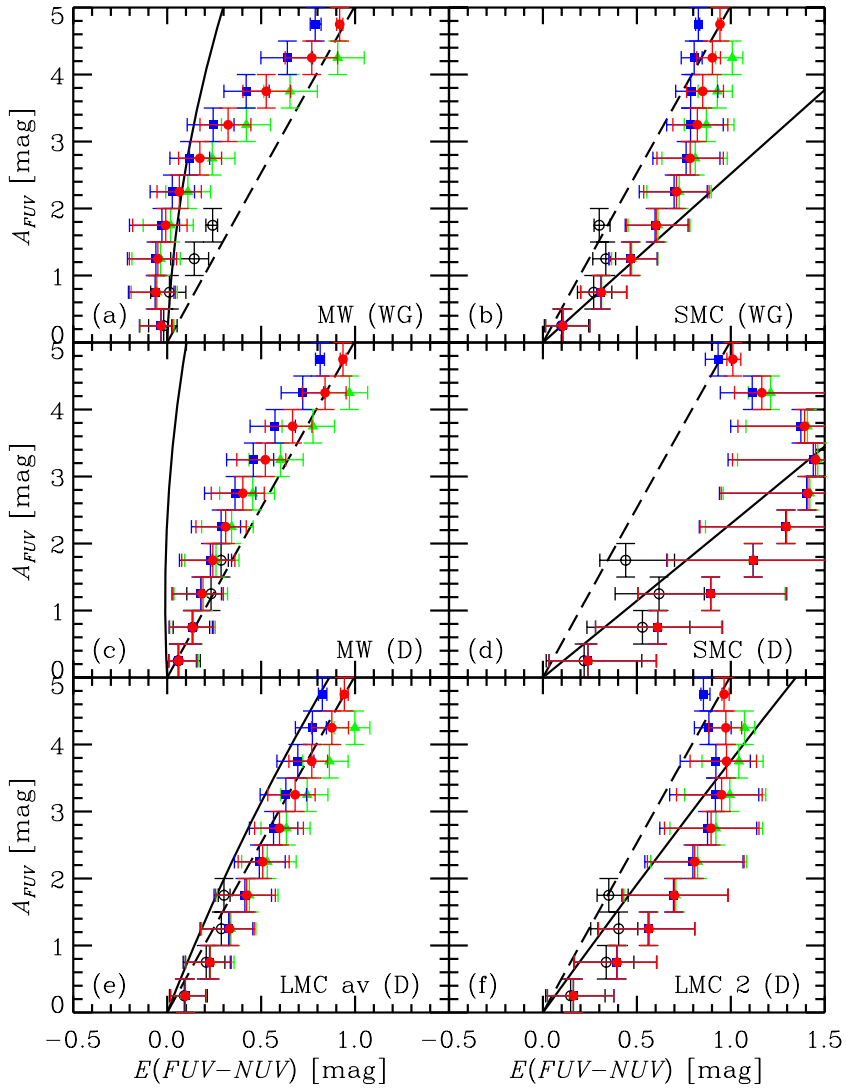

Figure 7. Same as Fig. 5, but the CCS model (Table 4) with different star formation histories. The open circles, filled triangles and filled circles are the cases with e-folding time-scales of 1, 3 and 5 Gyr, respectively. The filled squares are the cases with a constant star formation rate.

Fig. 7 shows the effect of the SFH on the E(FUV–NUV) $-A_{\rm FUV}$ relation for the CCS model. For an e-folding time-scale longer than 3 Gyr, the difference in E(FUV–NUV) is almost zero for $A_{\rm FUV} \lesssim 2$ mag, and small shifts ($\sim$0.1 mag) of the largest $A_{\rm FUV}$ are observed. This small difference is due to the small difference of the luminosity weights in the UV ($\lambda \lesssim 0.3$ μm) as shown in Fig. 4. On the other hand, a short e-folding time-scale like 1 Gyr produces a difference on the E(FUV–NUV) $-A_{\rm FUV}$ plane. This case reaches only $A_{\rm FUV} \lesssim 2$ mag because the radiation is dominated by the old population emitting from the outside of the dusty disc.

In summary, the effect on the *GALEX* colour significantly depends on the dust model (with/without the bump and the albedo) for a small UV attenuation, whereas it becomes independent of the dust model for the largest UV attenuation. The clumpy young stars and the intermediate population with a small scaleheight increase the UV attenuation. The effect of the intermediate population is larger than that of the young population, at least in the SFH considered here. On the other hand, the ISM clumpiness has a relatively small effect on the UV colour excess. The SFH has a very small effect on the UV colour excess if we assume a smooth SFH with an e-folding time-scale larger than 3 Gyr.

3.3 IR-to-UV flux ratio and *GALEX* colour

As shown in the previous section, the *GALEX* colour is very sensitive to the presence of the bump and the wavelength dependence of the albedo. Conversely, we may assess the dust models by comparing with the observed *GALEX* colours. Fig. 8 shows the diagram of the IRX (dust IR-to-UV flux ratio, $F_{\rm dust}/F_{\rm FUV}$) and the *GALEX* colour, FUV–NUV. The crosses and diamonds are the observed data of the nearby galaxies selected by NUV and FIR, respectively, taken from Buat et al. (2005) (see also Iglesias-Páramo et al. 2006). The filled circles and error-bars are made by the same procedure done in Fig. 5. We show only the CCS model with the e-folding time-scale of 5 Gyr for the comparison. We calculated the model dust IR flux as the total absorbed flux. This procedure is described in Appendix B. The UV flux is defined as the UV flux density multiplied by the effective wavelength of the UV filter. The solid and dashed lines in Fig. 8 are the loci expected from the extinction law and the Calzetti law, respectively.

By comparing the model points with the observed data, we assess which dust model is suitable for the observed galaxies. The SMC (WG dust) case shows a very good agreement with the data of the

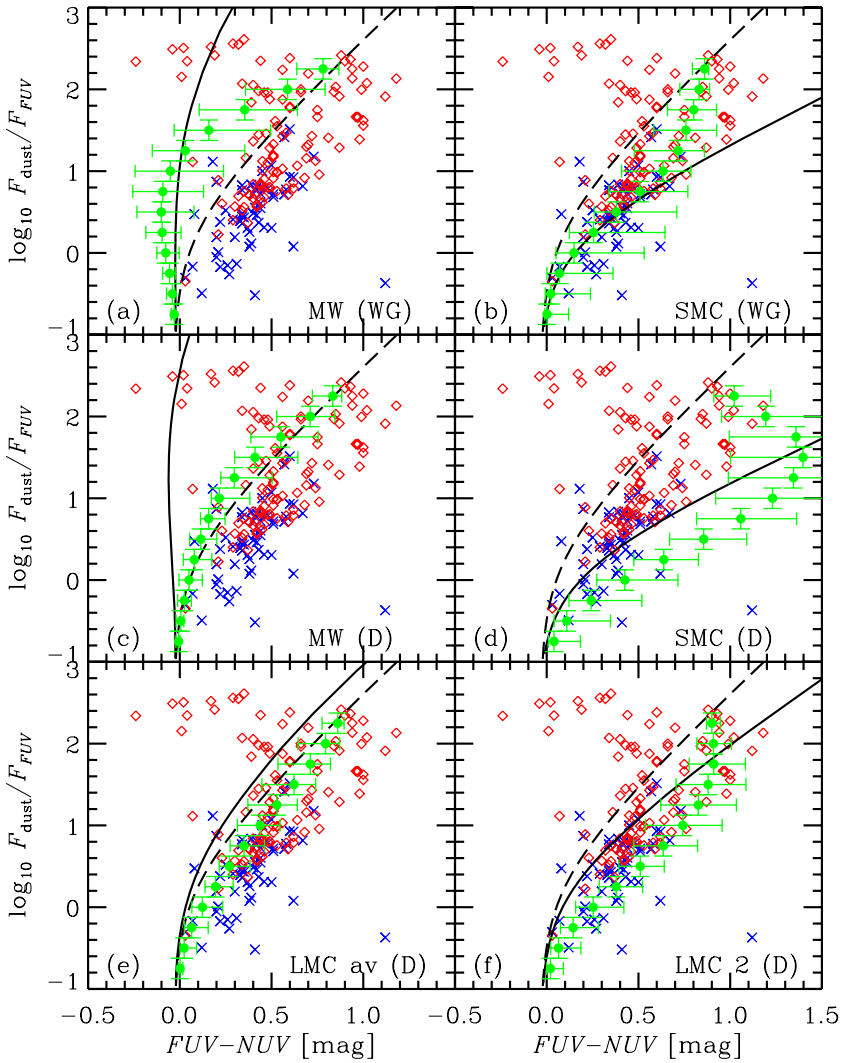

Figure 8. Dust IR-to-FUV flux ratio and the *GALEX* colour. The crosses and diamonds are observed data of the NUV-selected and the FIR-selected nearby galaxies, respectively, taken from Buat et al. (2005) (see also Iglesias-Páramo et al. 2006). The solid and dashed lines correspond to the extinction law and the Calzetti law, respectively. We show the CCS model (Table 4). The points predicted from the model are divided into several bins in the flux ratio. The vertical error-bars are the binwidth, the horizontal error-bars are the full width of the distribution of FUV–NUV in each bin, and the symbols are the median of the distribution.

UV-selected galaxies and the FIR-selected galaxies with $F_{\rm dust}/F_{\rm FUV} \lesssim 100$ (panel b). The LMC av (Draine dust) and the LMC 2 (Draine dust) cases are also compatible with the data (panels e and f). The colours predicted by the MW (Draine dust) case are still ∼0.2–0.3 mag bluer than the observed ones because of a strong bump and a shallow UV slope in the extinction law (panel c), although a different IMF like a Kroupa IMF could reduce the discrepancy (Panuzzo et al. 2006).[4] On the other hand, the predicted colours of the MW (WG dust) case are largely separated from the observed data, say ∼0.5 mag at $F_{\rm dust}/F_{\rm FUV} \sim 10$ (panel a). For the SMC (Draine dust) case (panel d), the predicted colours are too red (∼0.5 mag at $F_{\rm dust}/F_{\rm FUV} \sim 10$) because of a rapid decrease of the albedo between the two *GALEX* bands as shown in Fig. 1(b).

Interestingly, there is no model which reproduces the FIR-selected galaxies with $F_{\rm dust}/F_{\rm FUV} \gtrsim 100$ where ULIRGs also distribute (Goldader et al. 2002).[5] As discussed in Section 3.2, for an opaque disc, we expect to have an attenuation law (i.e. transmission rate curve) independent of dust properties. In fact, we find that the locations of the most opaque point in each panel are very similar; all dust models predict a very similar position on the diagram for $F_{\rm dust}/F_{\rm FUV} \gtrsim 100$. However, the real galaxies show a very large dispersion in the region.

Burgarella et al. (2005b) could not explain the same galaxies by their analysis either and suggested that an effect of 'decoupling' is important; the stellar populations producing the UV and the IR are completely different. For example, the UV radiation comes from

[4] Panuzzo et al. (2006) have reproduced the data of the NUV-selected galaxies with a Draine's MW dust (in a different version from this paper) better than here. This may be due to some differences between the two papers; they treat a two-dimensional disc plus bulge with a smooth medium, whereas we treat a one-dimensional plane-parallel disc with a clumpy medium. Moreover, a different age criterion of the intermediate population may play a role; Panuzzo et al. (2006) show that a shorter criterion gives a redder colour.

[5] Only a few galaxies in the FIR-selected sample of Buat et al. (2005) are ULIRGs.

the population outside the obscured region, whereas the population heating dust which emits the IR radiation is embedded there. In this case, the UV colour is decoupled with the UV attenuation traced by $F_{\rm dust}/F_{\rm FUV}$.[6] In the framework of this paper, such a 'decoupling' would take place if we consider an intermittent SFH. Now, we have three stellar populations: young and intermediate ones embedded in clumps and in the dusty disc, and old one distributed diffusely to the outside of the disc. Under an intermittent SFH with a time-scale longer than ∼300 Myr (age threshold between the intermediate and old populations), we can expect that the luminosity weights strongly vary along the time, and then the position of the most opaque case on the IRX–UV colour diagram would vary.

In summary, the *GALEX* data are consistent with WG's SMC dust and Draine's dusts with the bump (LMC av, LMC 2 and possibly MW). If we consider that the carrier of the UIR, very common among the nearby galaxies (e.g. Genzel & Cesarsky 2000), is also the bump carrier as suggested by some laboratory investigations (e.g. Sakata et al. 1983), dust with the bump is more favourable. For a flat wavelength dependence of the albedo like the WG dust, a strong bump seen in the MW makes the *GALEX* colour too blue. However, a weak bump like the LMC 2 type could be still compatible with the *GALEX* data. Some FIR-selected galaxies which have a large IR-to-UV flux ratio ($F_{\rm dust}/F_{\rm FUV} \gtrsim 100$) cannot be explained by a smooth SFH model, that may suggest their recent episodic star formation.

4 MEAN ATTENUATION LAWS

From the calculated transmission rate curves, we derive mean attenuation laws which would be useful for correcting the observed data of galaxies for the dust attenuation and for predicting the observable SEDs in theoretical works. We show only the CCS model (Table 4) in this section.

4.1 Mean UV-to-NIR attenuation laws

We find that the FUV attenuation, $A_{\rm FUV}$, represents the global shape of the attenuation laws. In Fig. 9, the colour excesses relative to $A_{\rm FUV}$ at various wavelengths, $E(\lambda - {\rm FUV}) = A_\lambda - A_{\rm FUV}$, are shown as a function of $A_{\rm FUV}$. To make the figure, we first averaged the transmission rates, T_λ, over the angle between a ray and the disc normal (i.e. inclination angle) via equation (B2). Then, we divided the inclination averaged T_λ into some bins in $A_{\rm FUV}$ and calculated the mean and the standard deviation in the distribution of $E(\lambda - {\rm FUV})$ in each bin and each dust model. The location of symbols and the vertical error-bars in Fig. 9 show the mean (not the median) and the standard deviation (not the full width), respectively. The horizontal error-bars indicate the binwidths. Fig. 9 shows that $E(\lambda - {\rm FUV})$ can be expressed as a function of $A_{\rm FUV}$ very nicely. Indeed, a typical standard deviation is as small as 0.1 mag. Thus, we tried to fit the calculated $E(\lambda - {\rm FUV})$ by a third-order polynomial function of $A_{\rm FUV}$ for each dust model as

$$E(\lambda - {\rm FUV}) = \alpha(\lambda) A_{\rm FUV} + \beta(\lambda) {A_{\rm FUV}}^2 + \gamma(\lambda) {A_{\rm FUV}}^3. \quad (5)$$

Note that we have assumed $E(\lambda - {\rm FUV}) = 0$ when $A_{\rm FUV} = 0$. The order of the polynomial function was determined, based on the Akaike's Information Criterion (Takeuchi 2000; Takeuchi, Yoshikawa & Ishii 2000); we tried to fit up to sixth order and confirmed that third order is enough. The resulting parameters for each wavelength and each dust model are tabulated in Appendix C. In Fig. 9, the fitting results are shown as thin solid curves.

Fig. 10 shows the mean attenuation laws obtained by the polynomial fit of $E(\lambda - {\rm FUV})$. We observe that the significance of the bump reduces as $A_{\rm FUV}$ increases (panels a, c, e and f). We also find a different slope in the UV ($1/\lambda \sim 5$–$7\ \mu{\rm m}^{-1}$) between the two SMC cases (panels b and d); a steeper rise of the SMC (Draine dust) case is due to a rapid decline of its albedo (Fig. 1b). We also note that the shape of the attenuation law for the most opaque case (top curves, $A_{\rm FUV} = 4$ mag) in each panel is very similar to those in other panels as discussed in Section 3.2.

We comment on the small feature seen at $1/\lambda \simeq 3.5\ \mu{\rm m}^{-1}$ in all panels of Fig. 10. This is due to the small feature seen in Fig. 4, the stellar Mg I λ2852 absorption line. This line is prominent in old stars' atmosphere but not in young and intermediate ones. Such an age-dependent strength of the line appears as a small feature in the luminosity fractions of young and intermediate stars. As discussed in Section 3.2, the wavelength dependence of the attenuation law (i.e. transmission rate T_λ) is determined by the luminosity fractions if the disc is enough opaque. Thus, such a stellar feature appears in the attenuation law of an opaque disc. Indeed, the feature in Fig. 10 is clearer for larger $A_{\rm FUV}$ cases. Interestingly, an age-dependent stellar feature can appear in the attenuation law through an age-selective attenuation.

To quantify the bump reduction and the slope change along the FUV attenuation seen in Fig. 10, we tried to fit the normalized mean attenuation laws by a power law plus a Gaussian bump in the same way as Burgarella et al. (2005b):

$$\frac{A_\lambda}{A_{\lambda_{\rm b}}} = (1 - B) \left(\frac{\lambda}{\lambda_{\rm b}} \right)^{-p} + B \exp \left(- \frac{\lambda - \lambda_{\rm b}}{\sigma} \right)^2, \quad (6)$$

where the bump position $\lambda_{\rm b} = 0.2175\ \mu$m and the bump width $\sigma = 0.02\ \mu$m. Although this function does not give a very good fit, we adopt it for simplicity. We left two free parameters: the power-law index p and the bump amplitude B. Fig. 11 shows results of the fit. We clearly find that the global slope of the attenuation law reduces as $A_{\rm FUV}$ increases (panel a). This is consistent with previous investigations (e.g. Ferrara et al. 1999; Városi & Dwek 1999; Witt & Gordon 2000; Pierini et al. 2004; Panuzzo et al. 2006). For each dust model, the power-law index decreases from a larger value than its extinction law (i.e. steeper attenuation) to a smaller value (i.e. greyer attenuation), and finally the indices converge a value similar to that of the Calzetti law ($p = 0.7$; see also Charlot & Fall 2000).

We also find a clear trend that the bump amplitude reduces as $A_{\rm FUV}$ increases (panel b); from a similar value to that in the extinction law to a very small amplitude, even less than that of the LMC 2 (Draine dust) case. Loci of the bump amplitudes along $A_{\rm FUV}$ are very similar, except for the LMC 2 (Draine dust) case whose amplitude is very small even in its extinction law. This trend is also consistent with the literature (e.g. Ferrara et al. 1999; Városi & Dwek 1999; Witt & Gordon 2000; Pierini et al. 2004; Panuzzo et al. 2006). The reduction of the bump amplitude is originated from the nature of the grey attenuation in an opaque disc as discussed in Section 3.1. Burgarella et al. (2005b) did not find the reduction of the bump amplitude along the FUV attenuation from their analysis of the galaxies observed with the *GALEX*. This may be because their sample consists of two different populations. Indeed, the bump amplitudes estimated in their analysis show a bimodal distribution.

[6] We can still rely on the IR-to-UV flux ratio for an indicator of the *total* UV attenuation because the flux ratio is the ratio of the absorbed to observed radiation energies (escaped from the obscured region plus emitted from the outside population) based on the energy conservation.

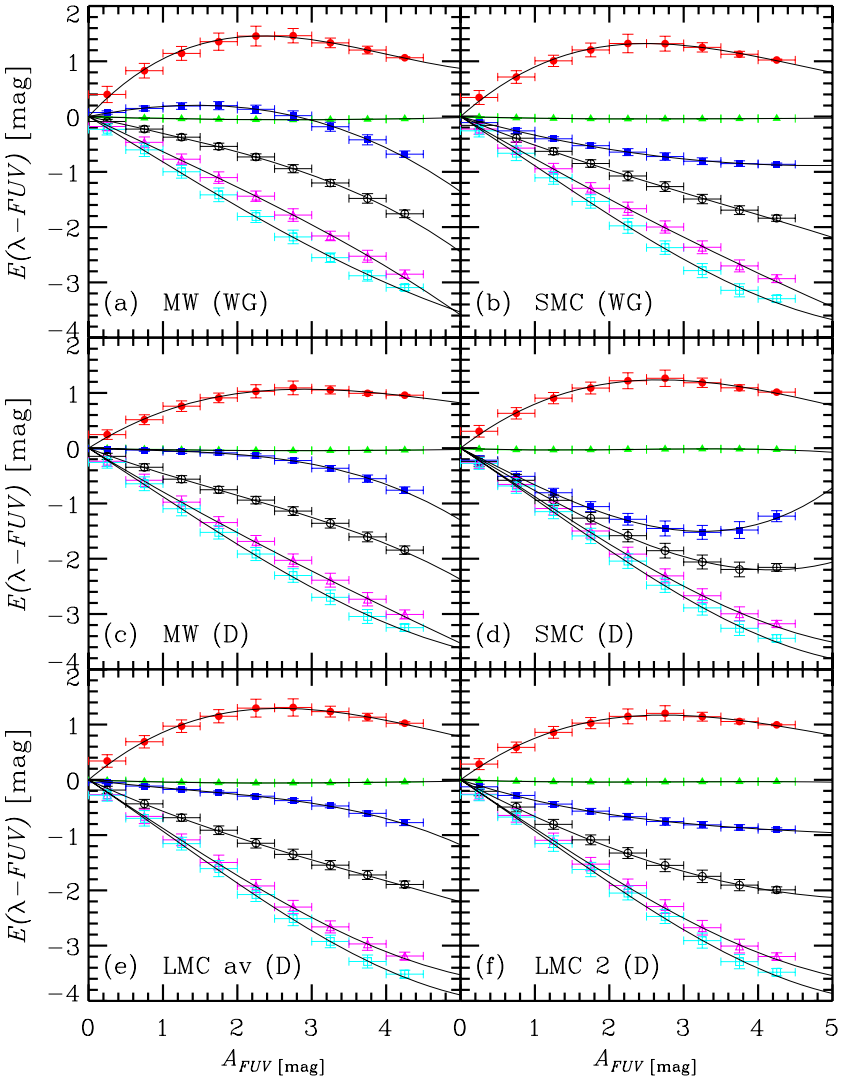

Figure 9. Colour excesses relative to the FUV at various wavelengths, $E(\lambda - \mathrm{FUV})$, as a function of the FUV attenuation, A_{FUV}. The filled circles, filled triangles, filled squares, open circles, open triangles and open squares are the colour excesses at $\lambda = 0.100, 0.157, 0.229, 0.300, 0.599$ and 1.19 μm, respectively. The horizontal error-bars indicate the A_{FUV} binwidth. The plotted points and the vertical error-bars are the mean and the standard deviation of the $E(\lambda - \mathrm{FUV})$ distribution in each bin. The thin solid curves are the third-order polynomial fits.

From Fig. 11, we understand why some dust models can reproduce the *GALEX* data in Fig. 8 and other can not. The slope of the attenuation law of the SMC (WG dust) is very good for the data. Suppose this as the reference case. Although the LMC av (Draine dust) and the LMC 2 (Draine dust) give a steeper slope than that of the SMC (WG dust), the bump which shifts the *GALEX* colour somewhat bluewards compensates the steepness. The slopes of the two MW dust cases are shallower than the reference SMC (WG dust) case, and moreover, there is the bump. For the SMC (Draine dust) which does not have the bump, the slope of the attenuation law is too steep.

4.2 Relations between UV attenuation and other quantities

We have derived the mean attenuation laws as a function of the FUV attenuation, A_{FUV}. If we have A_{FUV}, thus, we can obtain an attenuation law from the UV to the NIR. Now, we need to know relations between A_{FUV} and other observable or theoretical quantities in order to estimate A_{FUV}.

4.2.1 IR-to-UV flux ratio

The IR-to-UV flux ratio is a very good measure of A_{FUV} (Buat & Xu 1996; Gordon et al. 2000). This is because the relation is based on the energy conservation; the IR flux is the flux absorbed by dust grains. Thus, the relation is very robust against differences of the configuration of stars and dust and the dust model. Indeed, Fig. 12(a) shows the robustness of the relation against differences among dust models. The standard deviations are less than 0.2 mag. Since the FUV attenuation is defined as $A_{\mathrm{FUV}} = 2.5 \log (F^{\mathrm{int}}_{\mathrm{FUV}}/F_{\mathrm{FUV}})$ with $F^{\mathrm{int}}_{\mathrm{FUV}}$ and F_{FUV} being the intrinsic and observed FUV fluxes, respectively, we can express the relation as follows (e.g. Meurer et al. 1999):

$$A_{\mathrm{FUV}} = 2.5 \log \left(1 + \xi_{\mathrm{FUV}} \frac{F_{\mathrm{dust}}}{F_{\mathrm{FUV}}} \right), \tag{7}$$

where

$$\xi_{\mathrm{FUV}} = \frac{F^{\mathrm{int}}_{\mathrm{FUV}} - F_{\mathrm{FUV}}}{F_{\mathrm{dust}}}, \tag{8}$$

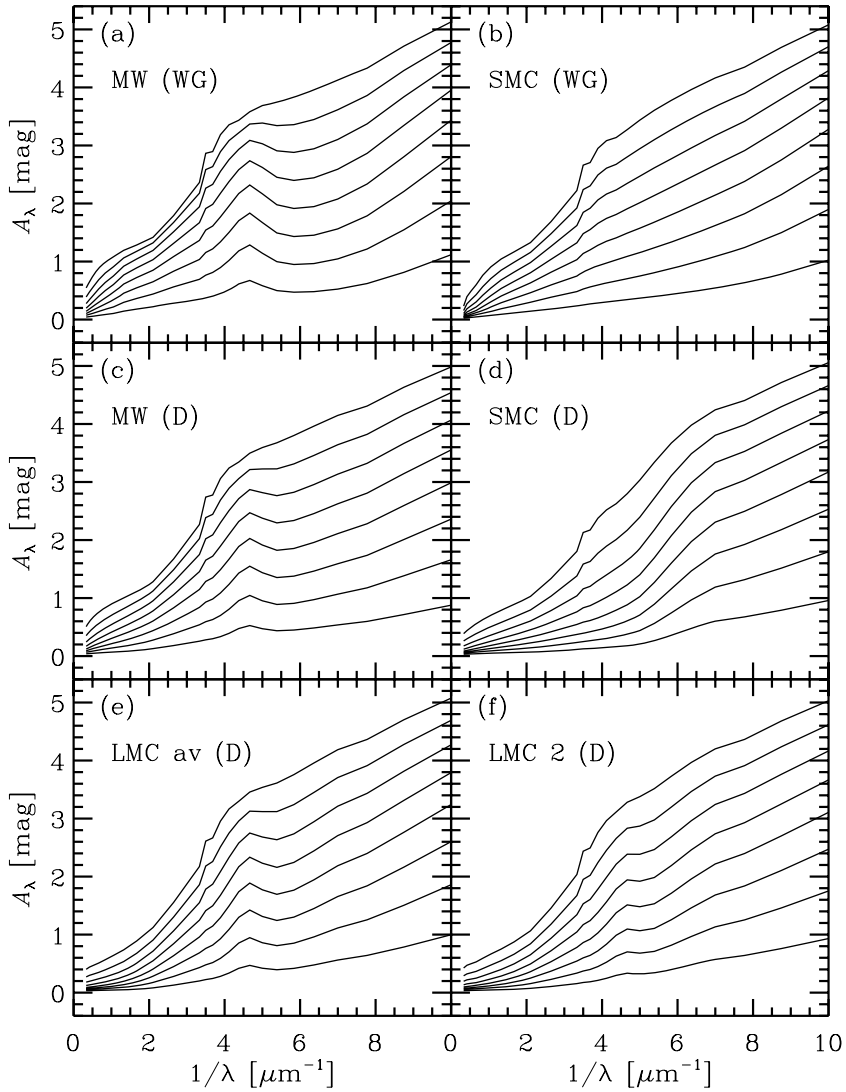

Figure 10. Mean attenuation laws. In each panel, eight attenuation laws are shown for $A_{\rm FUV} = 0.5$, 1.0, 1.5, 2.0, 2.5, 3.0, 3.5 and 4.0 mag from the bottom to the top.

which is the energy fraction of the absorbed FUV flux in the IR flux. From Fig. 12(b), we find that $\xi_{\rm FUV}$ is 0.3–0.6, although the value depends on the dust model and the dispersion is somewhat large. In an extremely dust-poor case ($F_{\rm dust}/F_{\rm FUV} \to 0$), $F^{\rm int}_{\rm FUV} = F_{\rm FUV}$, but still $F_{\rm dust} > 0$ because dust grains can be exposed by ionizing photons. Thus, $\xi_{\rm FUV} \to 0$ when $F_{\rm dust}/F_{\rm FUV} \to 0$. In the opposite limit, all stellar radiation is absorbed by dust and re-emitted in the IR ($F_{\rm FUV} \to 0$ and $F_{\rm dust} \to F_{\rm total}$, where $F_{\rm total}$ is the total flux); $\xi_{\rm FUV} \to \xi^{\infty}_{\rm FUV} \equiv F^{\rm int}_{\rm FUV}/F_{\rm total}$. If we assume the SED of a smooth exponential SFH with an e-folding time of 5 Gyr and a galactic age of 10 Gyr, we have $\xi^{\infty}_{\rm FUV} = 0.245$. With these limits, we have found a fitting function as

$$\xi_{\rm FUV} = \frac{\xi^{\infty}_{\rm FUV} {\rm e}^{x}}{1 + {\rm e}^{x}} + 0.400 \exp[-(0.591x - 0.185)^2], \quad (9)$$

where $x = \log(F_{\rm dust}/F_{\rm FUV})$. This is shown as the solid curve in Fig. 12(b). The relation obtained from equations (7) and (9) is also shown as solid curve in Fig. 12(a). The difference of the calibration obtained here from that of Buat et al. (2005) (dashed curve in Fig. 12a) is very small, except for the region of a small $F_{\rm dust}/F_{\rm FUV}$. Importantly, we can obtain a UV-to-NIR attenuation law from the observed IR-to-UV flux ratio with the calibration obtained here.

4.2.2 UV colour

As found by Meurer et al. (1999), the UV bright starburst galaxies show a tight correlation between the UV spectral slope (i.e. UV colour) and the IR-to-UV flux ratio (i.e. $A_{\rm FUV}$). However, normal galaxies do not follow the relation (Bell 2002; Kong et al. 2004; Buat et al. 2005). Figs 5 and 6 show that the relation between $A_{\rm FUV}$ and the *GALEX* colour excess strongly depends on the dust model. Thus, we expect that the UV colour and slope also depend on the dust model significantly. We estimated the UV slope β, where $f_\lambda \propto \lambda^\beta$, from the expected flux densities at 10 wavelength points between 0.12 and 0.26 μm listed in table 2 of Calzetti et al. (1994). As shown in Fig. 13, we find that relations between $A_{\rm FUV}$ and UV colour (or slope) show a large dispersion depending on the dust model. For example, $A_{\rm FUV}$ distributes from 0.5 to 4.0 mag for FUV–NUV = 0.5 mag or $\beta = -1$. Although we may expect a smaller dispersion

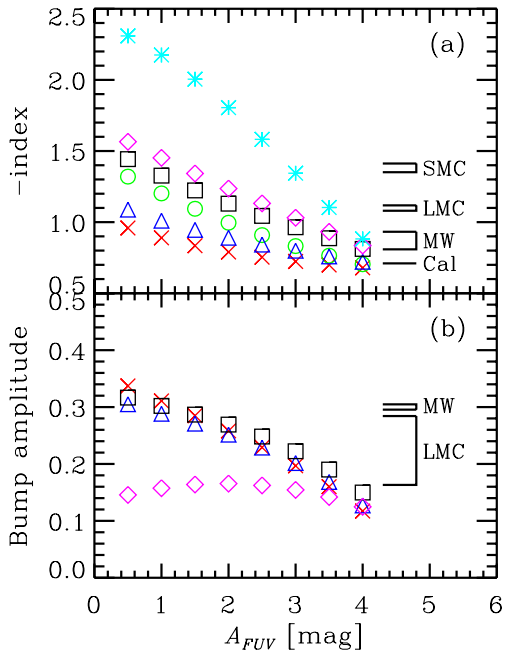

Figure 11. Properties of mean attenuation laws: (a) global slope of the attenuation law and (b) amplitude of the bump. The vertical axes are defined in equation (6): index $= -p$ and bump amplitude $= B$. The crosses and circles are MW (WG dust) and SMC (WG dust), respectively. The triangles, squares, diamonds and asterisks are MW (Draine dust), LMC av (Draine dust), LMC 2 (Draine dust) and SMC (Draine dust), respectively. For reference, the parameters of the extinction laws and the Calzetti law are marked in the right-hand side in each panel. Two marks for each extinction law mean two MW laws of WG dust and Drain dust, two LMC laws of the Draine dust and two SMC laws of WG dust and Draine dust.

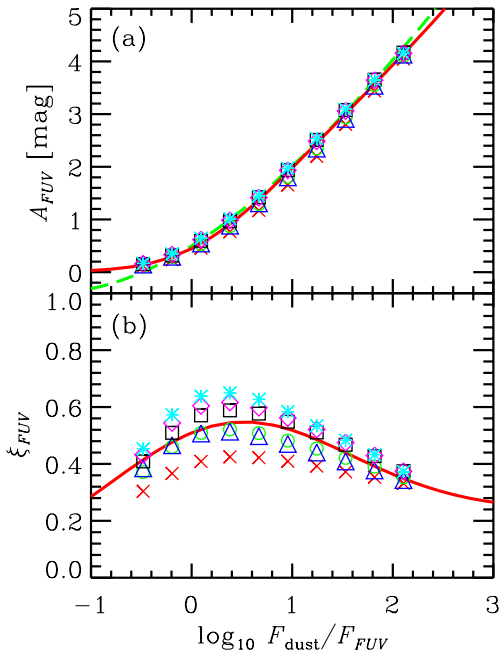

Figure 12. Mean relations between the IR-to-UV flux ratio and (a) the FUV attenuation and (b) the fraction of the FUV absorbed energy in the IR flux. The symbols, which almost overlap in the panel (a), indicate the mean relations for each dust model; crosses, circles, triangles, asterisks, squares and diamonds are MW (WG dust), SMC (WG dust), MW (Draine dust), SMC (Draine dust), LMC av (Draine dust) and LMC 2 (Draine dust), respectively. The solid lines are the best-fitting curves expressed in equations (7) and (9). The dashed line in the panel (a) is the calibration proposed by Buat et al. (2005).

of $A_{\rm FUV}$ for a fixed UV colour (or slope) in each dust model, the dispersion is still $\sim$1 mag.

4.2.3 Dust column density

To predict the observable fluxes of galaxies by theoretical models, we need a relation between $A_{\rm FUV}$ and a theoretical quantity. Since the total dust column density, $\Sigma_{\rm dust}$, of the disc can be calculated by a galactic chemical and dust amount evolution model (e.g. Inoue 2003), a relation between $A_{\rm FUV}$ and $\Sigma_{\rm dust}$ would be useful. Fig. 14 shows the $A_{\rm FUV}$–$\Sigma_{\rm dust}$ relation which is very robust against differences among dust models like the relation between $A_{\rm FUV}$ and the IR-to-UV flux ratio. A typical standard deviation is as small as 0.2 mag. As $\Sigma_{\rm dust}$ increases, first $A_{\rm FUV}$ increases linearly, and then becomes saturated at a certain value determined by the amount of the source outside of the disc, i.e. layering parameter (see Section 3.1). Taking into account such a behaviour, we fit the data by the following function:

$$A_{\rm FUV} = \sum_{i=1}^{3} a_i \{1 - \exp(-b_i \Sigma_{\rm dust})\}. \quad (10)$$

The resulting parameters are tabulated in Table 5, and the best-fitting curve is shown as the solid line in Fig. 14.

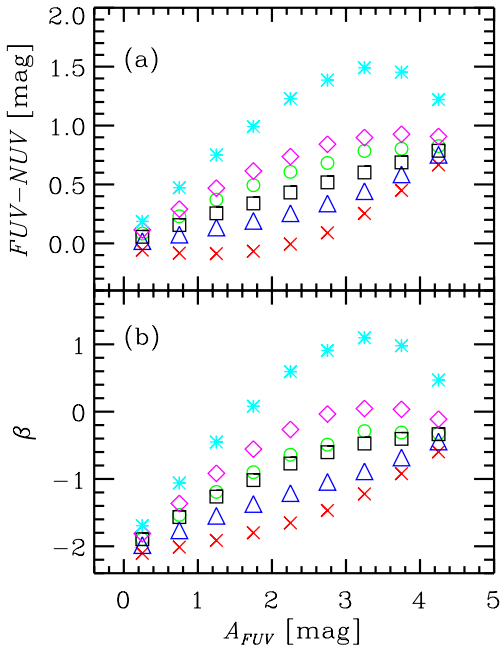

Figure 13. Mean relation between the FUV attenuation and the UV colour: (a) *GALEX* colour and (b) UV spectral slope β. The symbols are the same as in Fig. 12.

5 CONCLUSION

We discussed dust properties in the ISM of nearby normal galaxies observed through the *GALEX* FUV and NUV filters. To extract the dust properties from the *GALEX* data, we built a huge set of UV-to-NIR transmission rate curves of disc galaxies. The set covers a very wide range of the physical parameters of these galaxies. First, we examined various effects on the observed UV colour, such as the

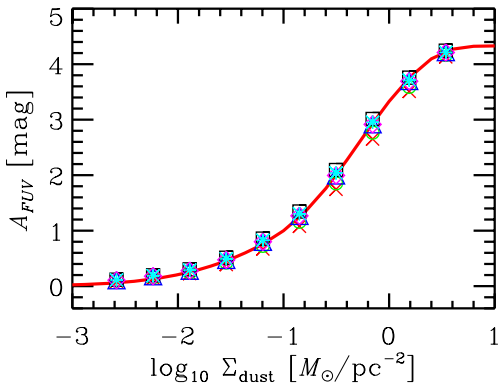

Figure 14. Mean relation between the FUV attenuation and the dust column density. The symbols are the same as in Fig. 12. The solid line is the best-fitting curve described in equation (10).

Table 5. Parameters for equation (10).

i	a_i	b_i
1	0.299	55.3
2	2.44	0.936
3	1.59	3.62

dust models, the age-selective attenuation including the clumpiness of stars, the clumpiness of the dust distribution and the SFH. Next, we compared the distribution of the observational data of nearby normal galaxies on the IR-to-UV flux ratio and the *GALEX* colour diagram with that expected from our transmission rate curves. Then, we derived UV-to-NIR mean attenuation laws as a function of the FUV attenuation from our transmission rate curves. We also derived relations between the FUV attenuation and the IR-to-UV flux ratio, the UV colour and the dust column density of the disc in order to use the mean attenuation laws practically.

From these analyses, we confirmed the following conclusions seen in the literature: the 2175-Å absorption bump, which is located in the *GALEX* NUV filter, makes UV colours much bluer (e.g. Gordon et al. 1997; Witt & Gordon 2000), the age-selective dust attenuation (i.e. younger stars are more attenuated) reduces the bump strength in the *attenuation law* (Granato et al. 2000; Panuzzo et al. 2006), the shape of the attenuation law changes from steep to shallow as the FUV attenuation increases (e.g. Witt & Gordon 2000), and the IR-to-UV flux ratio is a very good indicator of the FUV attenuation, whereas the UV colour is not good one (e.g. Buat & Xu 1996; Gordon et al. 2000).

Our new findings are as follows:

(i) A rapid decline of the albedo towards a short wavelength (except for the bump range) makes UV colours significantly redder (Sections 3.1 and 3.2),

(ii) A smooth exponential SFH with an e-folding time-scale larger than 3 Gyr does not affect the UV colour excess significantly (Section 3.2),

(iii) The FUV attenuation is a very good measure of the attenuation at an arbitrary wavelength from the UV to the NIR in our models (Section 4.1),

(iv) An age-dependent stellar feature like Mg I λ2752 can appear in the attenuation law through the age-selective attenuation (Section 4.1) and

(v) The dust column density shows a very tight relation with the FUV attenuation (Section 4.3).

From a comparison between our model and the *GALEX* observations in Section 3.3, we found that Witt & Gordon's SMC type dust shows a very good agreement with the *GALEX* data, whereas Witt & Gordon's MW type dust is not consistent with the data, and that Draine's LMC average and LMC 2 type dusts are also well compatible with the *GALEX* data, whereas Draine's SMC type dust is not consistent with the data. Draine's MW type dust gives slightly bluer colour than the data although this discrepancy could be resolved easily, for example, with another proper IMF as suggested by Panuzzo et al. (2006). Therefore, the main conclusion of this paper is given below.

(vi) In the ISM of the nearby normal galaxies, there is either dust with a bump and a smaller albedo for a shorter wavelength (except for the bump range), or dust without any bump but with an almost constant albedo.

If we regard very small carbonaceous grains responsible for the UIR emission band as the bump carrier (e.g. Whittet 2003), the former dust is more suitable for nearby normal galaxies, because the UIR emission is quite ubiquitous in these galaxies (Genzel & Cesarsky 2000).

Explaining the behaviour of the galaxies with a large IR-to-UV flux ratio (typically $\gtrsim$100) on the IR-to-UV flux ratio and the *GALEX* colour diagram remains a future work. Our model predicts the convergence to a certain *GALEX* colour independent of the dust model for galaxies with such a large IR-to-UV flux ratio, whereas the nature shows a very large dispersion of the colour. This may suggest a recent episodic star formation, which decouples the stellar populations observed in the UV and in the IR, in these galaxies.

ACKNOWLEDGMENTS

We appreciate the SSP spectra in electronic form provided by Alessandro Bressan and useful comments from the anonymous referee. AKI thanks Jean-Michel Deharveng for stimulating discussions and kind encouragement, and Takako T. Ishii for providing her IDL functions which are very useful for preparing figures. AKI also thanks all the members in the Laboratoire d'Astrophysique de Marseille for their very kind hospitality during his stay there. AKI and TTT were supported by the Japan Society for the Promotion of Science (JSPS) Postdoctoral Fellowships for Research Abroad (AKI: 2004 Apr.– 2005 Mar.; TTT: 2004 Apr.–2005 Dec.).

REFERENCES

Bell E. F., 2002, ApJ, 577, 150
Bianchi L., Clayton G. C., Bohlin R. C., Hutchings J. B., Massey P., 1996, ApJ, 471, 203
Binney J., Merrifield M., 1998, Galactic Astronomy. Princeton, NJ
Blitz L., Shu F. H., 1980, ApJ, 238, 148
Buat V., Xu C., 1996, A&A, 306, 61
Buat V. et al., 2005, ApJ, 619, L51
Burgarella D. et al., 2005a, ApJ, 619, L63
Burgarella D., Buat V., Iglesias-Páramo J., 2005b, MNRAS, 360, 1413
Burgh E. B., McCandliss S. R., Feldman P. D., 2002, ApJ, 575, 240
Calzetti D., 2001, PASP, 113, 1449
Calzetti D., Kinney A. L., Storchi-Bergmann T., 1994, ApJ, 429, 582
Calzetti D., Bohlin R. C., Gordon K. D., Witt A. N., Bianchi L., 1995, ApJ, 446, L97
Calzetti D. et al., 2005, ApJ, 633, 871
Charlot S., Fall S. M., 2000, ApJ, 539, 718

Cortese L. et al., 2006, ApJ, 637, 242
Dopita M. A. et al., 2005, ApJ, 619, 755
Draine B. T., 2003a, ARA&A, 41, 241
Draine B. T., 2003b, ApJ, 598, 1017
Engelbracht C. W., Gordon K. D., Rieke G. H., Werner M. W., Dale D. A., Latter W. B., 2005, ApJ, 628, L29
Ferrara A., Cimatti A., Bianchi S., Giovanardi C., 1999, ApJS, 123, 437
Field G. B., Goldsmith D. W., Habing H. J., 1969, ApJ, 155, L149
Fitzgerald M. P., Stephens T. C., Witt A. N., 1976, ApJ, 208, 709
Fitzpatrick E. L., 1986, AJ, 92, 1068
Fitzpatrick E. L., 1999, PASP, 111, 63
Genzel R., Cesarsky C. J., 2000, ARA&A, 38, 761
Gibson S. J., Nordsieck K. H., 2003, ApJ, 589, 362
Goldader J. D., Meurer G., Heckman T. M., Seibert M., Sanders D. B., Calzetti D., Steidel C. C., 2002, ApJ, 568, 651
Gordon K. D., 2004, in Witt, A. N., Clayton, G. C., Draine B. T., eds, ASP Conf. Ser. Vol. 309, Astrophysics of Dust. Astron. Soc. Pac., San Francisco, p. 77
Gordon K. D., 2005, in Popescu C. C., Tuffs R. J., eds, AIP Conf. Ser. vol. 761, The Spectral Energy Distribution of Gas-Rich Galaxies: Confronting Models with Data. p. 134
Gordon K. D., Clayton G. C., 1998, ApJ, 500, 816
Gordon K. D., Witt A. N., Carruthers G. R., Christensen S. A., Dohne B. C., 1994, ApJ, 432, 641
Gordon K. D., Calzetti D., Witt A. N., 1997, ApJ, 487, 625
Gordon K. D., Clayton G. C., Witt A. N., Misselt K. A., 2000, ApJ, 533, 236
Granato G. L., Lacey C. G., Silva L., Bressan A., Baugh C. M., Cole S., Frenk C. S., 2000, ApJ, 542, 710
Haikala L. K., Mattila K., Bowyer S., Sasseen T. P., Lampton M., Knude J., 1995, ApJ, 443, L33
Heckman T. M., Armus L., Weaver K. A., Wang J., 1999, ApJ, 517, 130
Henning Th., Jäger C., Mutschke H., 2004, in Witt A. N., Clayton G. C., Draine B. T., eds, ASP Conf. Ser. Vol. 309, Astrophysics of Dust. Astron. Soc. Pac., San Francisco, p. 603
Hirashita H., Buat V., Inoue A. K., 2003, A&A, 410, 83
Hobson M. P., Padman R., 1993, MNRAS, 264, 161
Hurwitz M., 1994, ApJ, 433, 149
Iglesias-Páramo J. et al., 2006, ApJS, 164, 381
Inoue A. K., 2001, AJ, 122, 1788
Inoue A. K., 2002, ApJ, 570, 688
Inoue A. K., 2003, PASJ, 55, 901
Inoue A. K., 2005, MNRAS, 359, 171
Inoue A. K., Hirashita H., Kamaya H., 2000, PASJ, 52, 539
Inoue A. K., Hirashita H., Kamaya H., 2001, ApJ, 555, 613
Kong X., Charlot S., Brinchmann J., Fall S. M., 2004, MNRAS, 349, 769
Lagache G. et al., 2004, ApJS, 154, 112
Laureijs R. J., Mattila K., Schnur G., 1987, A&A, 184, 269
Léger A., Puget J.-L., 1984, A&A, 137, L5
Léger A., Verstraete L., D'Hendecourt L., Défourneau D., Dutuit O., Schmidt W., Lauer J., 1989, in Allamandola L. J., Tielens A. G. G. M., eds, Proc. IAU Symp. 135, Kluwer Academic Publishers, Dordrecht, p. 173
Lehtinen K., Mattila K., 1996, A&A, 309, 570
Li A., Draine B. T., 2001, ApJ, 554, 778
Lillie C. F., Witt A. N., 1976, ApJ, 208, 64
Lord S. D., Hollenbach D. J., Haas M. R., Rubin R. H., Colgan S. W. J., Erickson E. F., 1996, ApJ, 465, 703
Martin C. D. et al., 2005, ApJ, 619, L1
Mathis J. S., 1973, ApJ, 186, 815
Mattila K., 1970, A&A, 9, 53
Mennella V., Colangeli L., Bussoletti E., Palumbo P., Rotundi A., 1998, ApJ, 507, L177
Meurer G. R., Heckman T. M., Calzetti D., 1999, ApJ, 521, 64
Misselt K. A., Clayton G. C., Gordon K. D., 1999, ApJ, 515, 128
Morgan D. H., Nandy K., Thompson G. I., 1976, MNRAS, 177, 531
Motta V. et al., 2002, ApJ, 574, 719
Murthy J., Im M., Henry R. C., Holberg J. B., 1993, ApJ, 419, 739
Murthy J., Henry R. C., 1995, ApJ, 448, 848
Myers P. C., 1978, ApJ, 225, 380
Neufeld D. A., 1991, ApJ, 370, L85
Noll S., Pierini D., 2005, A&A, 444, 137
Onaka T., 2004, in Witt A. N., Clayton G. C., Draine B. T., eds, ASP Conf. Ser. Vol. 309, Astrophysics of Dust. Astron. Soc. Pac., San Francisco, p. 163
Panuzzo P., Granato G. L., Buat V., Inoue A. K., Silva L., Iglesias-Paramo J., Bressan A. 2006, MNRAS, submitted
Pierini D., Gordon K. D., Witt A. N., Madsen G. J., 2004, ApJ, 617, 1022
Ponder J. M. et al., 1998, AJ, 116, 2297
Rana N. C., 1991, ARA&A, 29, 129
Robin A. C., Reylé C., Derrière S., Picaud S., 2003, A&A, 409, 523
Rocha-Pinto H. J., Flynn C., Scalo J., Hänninen J., Maciel W. J., Hensler G., 2004, A&A, 423, 517
Sakata A., Wada S., Okutsu Y., Shintani H., Nakada Y., 1983, Nat, 301, 493
Sakata A., Wada S., Tanabé T., Onaka T., 1984, ApJ, 287, L51
Schiminovich D., Friedman P. G., Martin C., Morrissey P. F., 2001, ApJ, 563, L161
Seibert M. et al., 2005, ApJ, 619, L55
Silva L., Granato G. L., Bressan A., Danese L., 1998, ApJ, 509, 103
Sofia U. J. et al., 2005, ApJ, 625, 167
Spitzer L., Schwarzschild M., 1951, ApJ, 114, 385
Takeuchi T. T., 2000, Ap&SS, 271, 213
Takeuchi T. T., Yoshikawa K., Ishii T. T., 2000, ApJS, 129, 1
Tinsley B. M., Larson R. B., 1978, ApJ, 221, 554
Tuffs R. J., Popescu C. C., Völk H. J., Kylafis N. D., Dopita M. A., 2004, A&A, 419, 821
Valencic L. A., Clayton G. C., Gordon K. D., Smith T. L., 2003, ApJ, 598, 369
Városi F., Dwek E., 1999, ApJ, 523, 265
Wada S., Kaito C., Kimura S., Ono H., Tokunaga A. T., 1999, A&A, 345, 259
Wang J., Hall P. B., Ge J., Li A., Schneider D. P., 2004, ApJ, 609, 589
Weingartner J. C., Draine B. T., 2001, ApJ, 548, 296
Whittet D. C. B., 2003, Dust in the Galactic Environment. Institute of Physics Publishing, Bristol
Whittet D. C. B., Shenoy S. S., Clayton G. C., Gordon K. D., 2004, ApJ, 602, 291
Witt A. N., Gordon K. D., 2000, ApJ, 528, 799
Witt A. N., Walker G. A. H., Bohlin R. C., Stecher T. P., 1982, ApJ, 261, 492
Witt A. N., Oliveri M. V., Schild R. E., 1990, AJ, 99, 888
Witt A. N., Petersohn J. K., Bohlin R. C., O'Connell R. W., Roberts M. S., Smith A. M., Stecher T. P., 1992, ApJ, 395, L5
Witt A. N., Petersohn J. K., Holberg J. B., Murthy J., Dring A., Henry R. C., 1993, ApJ, 410, 714
Witt A. N., Friedmann B. C., Sasseen T. P., 1997, ApJ, 481, 809
Wolfire M. G., McKee C. F., Hollenbach D., Tielens A. G. G. M., 2003, ApJ, 587, 278
Wood D. O. S., Churchwell E., 1989, ApJ, 340, 265
Zaritsky D., Harris J., Thompson I. B., Grebel E. K., 2004, AJ, 128, 1606

APPENDIX A: CLUMPY STELLAR EMISSIVITY

Here, we describe how to manage clumpiness of the stellar emissivity. We do not consider any systematic distribution of clumps, i.e. clumps distribute uniformly in the gas plus dust disc. However, we consider that a mean number density of embedded stars decreases along the vertical axis of the disc. We update the treatment of the clumpy stellar emissivity of the section 3.4.1 in Inoue (2005) as follows.

First, we normalize the intrinsic emissivity, η_*, as unity. When clumps exist only within the gas plus dust disc of the half height $h_{\rm d}$ and the embedded stars exist only in clumps, this normalization

becomes

$$\int_{-h_{\rm d}}^{h_{\rm d}} \eta_*(z)\,{\rm d}z = 1. \tag{A1}$$

If the number distribution of the embedded stars is an exponential function along the vertical axis, z, with an e-folding scale of h_*, we have $\eta_*(z) = \exp(-|z|/h_*)/2h_*[1 - \exp(-h_{\rm d}/h_*)]$ for $|z| \leqslant h_{\rm d}$, otherwise $\eta_* = 0$.

A part of the radiation from the embedded stars is locally absorbed by dust in the clump where the stars are embedded. If the embedded stars distribute uniformly in the clump and the scattering by dust is isotropic, the photon escape probability from the clump, $P_{\rm esc}(\tau_{\rm cl}, \omega_{\rm cl})$, with the optical depth radius $\tau_{\rm cl}$ and the effective albedo $\omega_{\rm cl}$, is given by equation (10) in Inoue (2005). Therefore, the clumpy stellar emissivity input into the transfer equation is

$$\eta_*^{\rm cl}(z) = \begin{cases} \frac{P_{\rm esc}(\tau_{\rm cl},\omega_{\rm cl})\exp(-|z|/h_*)}{2h_*\{1-\exp(-h_{\rm d}/h_*)\}} & (\text{for} \quad |z| < h_d) \\ 0 & (\text{for} \quad |z| > h_d) \end{cases}. \tag{A2}$$

In this case, we do not have any incident radiation at the top of the disc as the upper boundary condition of the calculation. In addition, we set a mirror boundary condition at the equatorial plane of the disc.

APPENDIX B: ESTIMATION OF THE DUST IR LUMINOSITY

Here, we explain the estimation procedure of the dust IR luminosity, in other words, the total absorbed luminosity. The dust IR luminosity is expressed as (e.g. Inoue, Hirashita & Kamaya 2000)

$$L_{\rm dust} = L_{{\rm Ly}\alpha} + (1 - f_{\rm LC})L_{\rm LC} + \int_{\lambda_{\rm L}}^{\infty} L_\lambda(1 - \langle T_\lambda \rangle)\,{\rm d}\lambda, \tag{B1}$$

where $L_{{\rm Ly}\alpha}$ and $L_{\rm LC}$ are the Lyα emission line and the Lyman continuum luminosities, L_λ is the intrinsic luminosity density of all stellar populations, $f_{\rm LC}$ is the luminosity fraction of the Lyman continuum absorbed by hydrogen atoms and $\langle T_\lambda \rangle$ is the transmission rate averaged over the angle between the disc normal and a ray. That is,

$$\langle T_\lambda \rangle = \int_0^1 T_\lambda(\mu)\,{\rm d}\mu, \tag{B2}$$

μ is the cosine of the angle. Note that we should integrate the *composite* transmission rate (with an angle dependence) over the angle to obtain the total absorbed energy within the disc. We assume the same SED as that used to obtain the luminosity weights in equation (1) and Fig. 4 (solid lines). The first two terms in equation (B1) can be reduced to $(1 - \alpha f_{\rm LC})\,L_{\rm LC}$ with α is a numerical factor of the order of unity (e.g. Inoue et al. 2000). With the case B approximation and the assumed SED, we have $\alpha \simeq 0.6$. Some estimates suggest $f_{\rm LC} \simeq 0.5$ (Inoue, Hirashita & Kamaya 2001; Inoue 2001, 2002; Hirashita, Buat & Inoue 2003). Thus, we adopt $1 - \alpha f_{\rm LC} = 0.7$. This choice does not affect the estimated dust IR luminosity significantly because a typical luminosity fraction of $L_{\rm LC}$ in the total luminosity is small enough (15 per cent).

APPENDIX C: PARAMETERS FOR MEAN ATTENUATION LAWS

We summarize the fitting parameters for equation (5) of each dust model in Tables C1–C6.

Table C1. Parameters for MW (WG dust).

λ (μm)	α	β	γ
0.100	1.443E+00	−4.356E-01	3.637E-02
0.114	7.122E-01	−1.762E-01	1.066E-02
0.129	2.658E-01	−5.189E-02	1.559E-03
0.143	5.388E-02	−9.868E-03	1.126E-03
0.157	−4.344E-02	8.463E-03	−1.066E-04
0.171	−6.372E-02	1.537E-02	−2.479E-03
0.186	−6.457E-03	9.752E-03	−5.950E-03
0.200	1.872E-01	−3.753E-02	−7.192E-03
0.214	4.086E-01	−1.208E-01	−1.885E-03
0.229	2.693E-01	−8.075E-02	−5.494E-03
0.243	4.049E-02	−1.150E-02	−9.710E-03
0.257	−1.145E-01	2.076E-02	−1.076E-02
0.271	−2.049E-01	2.850E-02	−1.158E-02
0.286	−2.642E-01	3.982E-02	−1.117E-02
0.300	−3.191E-01	2.379E-02	−1.160E-02
0.378	−4.347E-01	6.473E-03	−8.980E-03
0.475	−5.609E-01	7.314E-03	−7.126E-03
0.599	−6.473E-01	1.715E-02	−6.257E-03
0.754	−7.206E-01	2.182E-02	−4.276E-03
0.949	−7.969E-01	1.269E-02	9.968E-04
1.194	−8.273E-01	−2.497E-03	5.293E-03
1.504	−8.508E-01	−1.808E-02	8.990E-03
1.893	−8.700E-01	−3.024E-02	1.135E-02
2.383	−8.848E-01	−3.682E-02	1.219E-02
3.000	−8.984E-01	−3.935E-02	1.202E-02

Table C2. Parameters for SMC (WG dust).

λ (μm)	α	β	γ
0.100	1.207E+00	−3.332E-01	2.472E-02
0.114	6.343E-01	−1.435E-01	7.019E-03
0.129	2.923E-01	−5.089E-02	−7.859E-05
0.143	9.794E-02	−1.118E-02	−7.718E-04
0.157	−4.001E-02	1.132E-02	−8.986E-04
0.171	−1.454E-01	2.428E-02	−4.576E-04
0.186	−2.226E-01	3.206E-02	−2.444E-04
0.200	−2.871E-01	3.780E-02	−3.013E-04
0.214	−3.344E-01	4.106E-02	−7.320E-04
0.229	−3.786E-01	4.194E-02	−3.141E-04
0.243	−4.069E-01	3.710E-02	1.830E-03
0.257	−4.429E-01	3.767E-02	1.865E-03
0.271	−4.820E-01	4.311E-02	−8.637E-04
0.286	−5.139E-01	3.827E-02	1.631E-03
0.300	−5.605E-01	4.701E-02	−4.466E-03
0.378	−6.488E-01	3.886E-02	−5.286E-03
0.475	−7.278E-01	2.905E-02	−3.543E-03
0.599	−7.841E-01	1.859E-02	1.004E-04
0.754	−8.222E-01	4.153E-03	4.159E-03
0.949	−8.521E-01	−1.531E-02	8.775E-03
1.194	−8.728E-01	−3.147E-02	1.182E-02
1.504	−8.927E-01	−4.005E-02	1.268E-02
1.893	−9.059E-01	−4.106E-02	1.204E-02
2.383	−9.178E-01	−3.951E-02	1.089E-02
3.000	−9.379E-01	−3.338E-02	8.090E-03

Table C3. Parameters for MW (Draine dust).

λ (μm)	α	β	γ
0.100	8.548E-01	−2.088E-01	1.413E-02
0.114	4.825E-01	−1.044E-01	5.833E-03
0.129	2.151E-01	−4.025E-02	1.456E-03
0.143	8.084E-02	−1.464E-02	9.074E-04
0.157	−3.413E-02	7.360E-03	−2.950E-04
0.171	−1.147E-01	2.546E-02	−2.297E-03
0.186	−1.448E-01	4.049E-02	−6.133E-03
0.200	−7.306E-02	3.724E-02	−1.109E-02
0.214	5.246E-02	5.592E-03	−1.254E-02
0.229	−6.209E-02	3.145E-02	−1.423E-02
0.243	−2.465E-01	6.706E-02	−1.321E-02
0.257	−3.671E-01	7.848E-02	−1.139E-02
0.271	−4.389E-01	8.058E-02	−1.184E-02
0.286	−4.776E-01	8.018E-02	−9.885E-03
0.300	−5.207E-01	7.287E-02	−1.274E-02
0.378	−6.643E-01	5.906E-02	−9.598E-03
0.475	−7.638E-01	4.535E-02	−6.066E-03
0.599	−8.198E-01	3.164E-02	−1.767E-03
0.754	−8.487E-01	1.481E-02	2.467E-03
0.949	−8.626E-01	−2.464E-03	6.332E-03
1.194	−8.707E-01	−1.802E-02	9.473E-03
1.504	−8.769E-01	−3.025E-02	1.170E-02
1.893	−8.835E-01	−3.866E-02	1.296E-02
2.383	−8.918E-01	−4.312E-02	1.328E-02
3.000	−9.019E-01	−4.409E-02	1.281E-02

Table C4. Parameters for LMC av (Draine dust).

λ (μm)	α	β	γ
0.100	1.140E+00	−3.017E-01	2.097E-02
0.114	6.430E-01	−1.445E-01	6.918E-03
0.129	3.107E-01	−5.632E-02	3.382E-04
0.143	1.327E-01	−1.758E-02	−9.865E-04
0.157	−5.417E-02	1.508E-02	−1.054E-03
0.171	−1.805E-01	3.349E-02	−8.935E-04
0.186	−2.348E-01	4.734E-02	−3.223E-03
0.200	−1.839E-01	5.265E-02	−8.902E-03
0.214	−7.520E-02	3.457E-02	−1.243E-02
0.229	−1.851E-01	5.198E-02	−1.240E-02
0.243	−3.571E-01	6.668E-02	−7.398E-03
0.257	−4.713E-01	6.447E-02	−2.996E-03
0.271	−5.439E-01	6.472E-02	−3.028E-03
0.286	−5.781E-01	5.665E-02	2.720E-04
0.300	−6.281E-01	6.490E-02	−5.516E-03
0.378	−7.637E-01	4.383E-02	−1.448E-03
0.475	−8.453E-01	1.703E-02	3.602E-03
0.599	−8.781E-01	−1.221E-02	9.342E-03
0.754	−8.903E-01	−3.086E-02	1.237E-02
0.949	−8.952E-01	−4.055E-02	1.361E-02
1.194	−8.994E-01	−4.538E-02	1.391E-02
1.504	−9.034E-01	−4.714E-02	1.372E-02
1.893	−9.065E-01	−4.725E-02	1.333E-02
2.383	−9.094E-01	−4.650E-02	1.284E-02
3.000	−9.141E-01	−4.493E-02	1.214E-02

Table C5. Parameters for LMC 2 (Draine dust).

λ (μm)	α	β	γ
0.100	9.849E-01	−2.498E-01	1.699E-02
0.114	5.809E-01	−1.278E-01	6.279E-03
0.129	3.089E-01	−5.578E-02	3.272E-04
0.143	1.549E-01	−2.023E-02	−1.482E-03
0.157	−4.878E-02	1.837E-02	−2.057E-03
0.171	−2.238E-01	4.130E-02	−5.816E-04
0.186	−3.441E-01	5.403E-02	4.379E-04
0.200	−3.839E-01	6.664E-02	−2.391E-03
0.214	−3.658E-01	7.510E-02	−7.153E-03
0.229	−4.411E-01	7.418E-02	−4.840E-03
0.243	−5.344E-01	5.563E-02	3.301E-03
0.257	−5.998E-01	4.137E-02	7.775E-03
0.271	−6.490E-01	4.151E-02	6.645E-03
0.286	−6.673E-01	2.952E-02	9.911E-03
0.300	−7.130E-01	4.771E-02	1.951E-03
0.378	−8.037E-01	2.841E-02	3.376E-03
0.475	−8.581E-01	7.700E-03	5.843E-03
0.599	−8.795E-01	−1.402E-02	9.644E-03
0.754	−8.883E-01	−2.872E-02	1.194E-02
0.949	−8.928E-01	−3.802E-02	1.319E-02
1.194	−8.973E-01	−4.311E-02	1.359E-02
1.504	−9.019E-01	−4.537E-02	1.349E-02
1.893	−9.041E-01	−4.566E-02	1.320E-02
2.383	−9.065E-01	−4.516E-02	1.280E-02
3.000	−9.120E-01	−4.371E-02	1.207E-02

Table C6. Parameters for SMC (Draine dust).

λ (μm)	α	β	γ
0.100	1.043E+00	−2.622E-01	1.688E-02
0.114	6.491E-01	−1.392E-01	5.393E-03
0.129	3.831E-01	−6.501E-02	−1.364E-03
0.143	2.148E-01	−2.229E-02	−4.045E-03
0.157	−5.989E-02	3.263E-02	−4.722E-03
0.171	−3.110E-01	5.495E-02	5.624E-04
0.186	−4.910E-01	4.419E-02	9.322E-03
0.200	−5.982E-01	2.121E-02	1.698E-02
0.214	−6.509E-01	5.248E-03	2.060E-02
0.229	−6.788E-01	−9.267E-03	2.328E-02
0.243	−6.912E-01	−3.038E-02	2.766E-02
0.257	−7.093E-01	−3.737E-02	2.829E-02
0.271	−7.358E-01	−2.737E-02	2.429E-02
0.286	−7.384E-01	−3.690E-02	2.616E-02
0.300	−7.807E-01	−4.948E-03	1.573E-02
0.378	−8.308E-01	−1.032E-03	1.058E-02
0.475	−8.621E-01	−4.739E-03	8.648E-03
0.599	−8.740E-01	−1.698E-02	1.029E-02
0.754	−8.810E-01	−2.857E-02	1.204E-02
0.949	−8.860E-01	−3.811E-02	1.341E-02
1.194	−8.912E-01	−4.398E-02	1.398E-02
1.504	−8.970E-01	−4.654E-02	1.390E-02
1.893	−9.034E-01	−4.678E-02	1.339E-02
2.383	−9.100E-01	−4.562E-02	1.263E-02
3.000	−9.166E-01	−4.365E-02	1.175E-02

This paper has been typeset from a TEX/LATEX file prepared by the author.